Endothelial sensing of AHR ligands regulates intestinal homeostasis

Benjamin G. Wiggins (bwiggins@ic.ac.uk)
Imperial College London https://orcid.org/0000-0001-5215-2004
Yi-Fang Wang
MRC London Institute of Medical Sciences
Alice Burke
Imperial College London
Nil Grunberg
Imperial College London
Julia M. Vlachaki Walker
MRC London Institute of Medical Sciences
Marian Dore
MRC London Institute of Medical Sciences
Catherine Chahrour
MRC London Institute of Medical Sciences
Betheney Pennycook
MRC London Institute of Medical Sciences
Julia Sanchez-Garrido
Imperial College London
Santiago Vernia
MRC London Institute of Medical Sciences
Alexis R. Barr
MRC London Institute of Medical Sciences
Gad Frankel
Imperial College London
Graeme M. Birdsey
Imperial College London
Anna M. Randi
Imperial College London
Chris Schiering (cschieri@ic.ac.uk)
Imperial College London

Research Article

Keywords: aryl hydrocarbon receptor, endothelial cells, scRNAseq

Posted Date: April 11th, 2023

DOI: https://doi.org/10.21203/rs.3.rs-2784958/v1

Version of Record: A version of this preprint was published at Nature on August 16th, 2023. See the published version at https://doi.org/10.1038/s41586-023-06508-4.

Abstract

The blood and lymphatic vasculature is lined by functionally specialised endothelial cells (ECs). Vascular beds act as an essential physical barrier, control nutrient transport, facilitate tissue immunosurveillance, and coordinate angiogenesis and lymphangiogenesis to ensure appropriate tissue perfusion and drainage[1,2]. Conversely, vascular maladaptation can lead to pathological angiogenesis and the perpetuation of inflammation in chronic inflammatory diseases[3,4]. In the intestine, dietary and microbial cues are particularly important in regulation of organ homeostasis. However, whether enteric ECs actively sense and integrate such signals is currently unknown. Here, we show that the aryl hydrocarbon receptor (AHR), a ligand-activated transcription factor, acts as critical node for EC-sensing of dietary metabolites in adult mice and human primary ECs. We first established a comprehensive single-cell endothelial atlas of the mouse small intestine, uncovering the cellular complexity and functional heterogeneity of blood and lymphatic ECs. Analyses of AHR mediated responses at single-cell resolution identified tissue-protective transcriptional signatures and regulatory networks promoting cellular quiescence and vascular normalcy at steady state. Endothelial AHR-deficiency in adult mice resulted in dysregulated inflammatory responses, and initiation of proliferative and angiogenic pathways. Furthermore, endothelial sensing of dietary AHR ligands was required for optimal protection against enteric infection. In human ECs, AHR signalling promoted quiescence and restrained activation by inflammatory mediators. Together, our data provide a comprehensive dissection of the impact of environmental sensing across the spectrum of enteric endothelia, demonstrating that endothelial AHR signalling integrates dietary cues to maintain tissue homeostasis by promoting EC quiescence and normalcy.

Main

Recent advances in single-cell sequencing technologies have led to increased appreciation of EC cellular and functional diversity within vascular beds (arteries, capillaries, veins, lymphatics) and have highlighted tissue origin as a critical determinant of EC heterogeneity[5–8]. Physiological aspects of enteric vasculature (e.g. lipid absorption, nutrient transport, cellular trafficking) have been studied in detail; however, little attention has been paid to EC heterogeneity, functional specialisation and tissue-specific adaptations. ECs are long-lived and exist in a state of functional quiescence, allowing them to be rapidly activated by inflammatory stimuli or tissue injury[1]. The signals regulating EC quiescence and vascular normalcy at the intestinal barrier, which is constantly exposed to a plethora of commensal microorganisms, pathogens, and dietary factors, remain elusive. Identification of such environmental cues that actively enforce EC quiescence and contain EC activation would aid our understanding of vascular control of intestinal homeostasis and pathophysiology.

The AHR, a ligand-activated transcription factor capable of sensing dietary micronutrients, pathogen-derived molecules and microbial metabolites, plays an essential role in maintaining intestinal homeostasis[9]. Genetic deficiency in AHR is associated with compromised intestinal barrier integrity, altered microbiota composition, and dysregulated host responses to pathogens and injury[10–13].

Furthermore, genome-wide association studies have identified *AHR* as a susceptibility locus in inflammatory bowel disease[14], highlighting the relevance of this pathway to human disease. In recent years, studies have almost exclusively focused on the role of AHR in intestinal immune cells but increasing evidence points to an important function of AHR in structural cells[12,15]. Although its role in enteric ECs remains unexplored, the AHR pathway has been linked to vascular biology. AHR deficiency results in a number of developmental vascular defects in the liver, heart, kidney and eye[16–18], and is associated with hypotension[19]. Within the vasculature, laminar fluid shear stress is a potent activator of the AHR pathway[20,21], and endothelial cells can sense and respond to AHR ligands *in vitro*[22–24].

Here we used single-cell RNA sequencing (scRNAseq) to dissect the transcriptomic responses to AHR pathway activation across blood and lymphatic EC populations of the adult mouse small intestine, revealing substantial cellular heterogeneity within the enteric vascular bed. AHR signalling in mouse and human cells limited EC activation via inhibiting proliferative and pro-inflammatory pathways; while AHR-deficiency or lack of dietary AHR ligands resulted in endothelial activation, proliferation, and contributed to an increased susceptibility to intestinal bacterial infection. Our study demonstrates a requirement for AHR-mediated environmental sensing in enteric ECs for the maintenance of endothelial quiescence.

Enteric vasculature at single-cell resolution

To gain a deeper understanding of cellular complexity of the small intestinal (SI) blood and lymphatic vasculature, we performed scRNAseq on total small intestine (SI) ECs. Wild-type (WT) mice were acutely (3h) exposed to AHR ligand 6-Formylindolo(3,2-*b*)carbazole (FICZ) or vehicle, before total ECs ($CD31^{+}CD45^{-}$) were sorted and sequenced (**Extended Data** Fig. 1a). After filtering, doublet exclusion, and removal of contaminant clusters (**Extended Data** Fig. 1b; **Table S1**; **Methods**), our dataset comprised 21,117 high quality enteric endothelial cells. Prior to analysis of AHR transcriptional responses, we performed an integrated analysis of the combined dataset (vehicle & ligand) to construct a small intestinal EC atlas. Combined, we revealed 11 endothelial clusters, clearly demarcated across two superclusters: lymphatic endothelial cells (LEC) and blood endothelial cells (BEC; Fig. 1a-b). Analyses of known markers of BEC (*Bcam, Esam, Ly6c1, Ly6a, Cd36, Sox17, Nrp1, Vwf, Plvap*) and LEC (*Prox1, Lyve1, Pdpn, Thy1, Mmrn1, Prss23, Fxyd6, Cp, Nrp2*) confirmed supercluster identity (**Extended Data** Fig. 1c-d), and our data contained negligible contamination from epithelial cells (*Epcam*), mural cell types (*Acta2, Pdgfrb*), fibroblasts (*Col1a1*), erythrocytes (*Hba-a1, Hba-a2, Hbb-bs*), and immune cells (*Ptprc*) (**Extended Data** Fig. 1.**e**)[7]. Cluster annotation was based on known marker gene expression[5,6], beginning with nomenclature from a recent murine endothelial atlas[7]. Hierarchical clustering showed clear demarcation at the gene level, with LEC2a and LEC1 showing most similarities (**Extended Data** Fig. 1f), and our LEC clusters were most congruent with capillary, rather than larger collecting vessel, or valve lymphatics recently identified in mesenteric adipose (**Extended Data** Fig. 1g)[6].

Alongside the examination of enriched marker genes within each cluster (**Extended Data** Fig. 2a; **Table S2**), we took a two-step approach to better understand how endothelial heterogeneity shapes biological

function. First, to gain a deeper insight into the putative biological roles of EC clusters, we performed pathway and gene set overdispersion analysis (Pagoda2) on each supercluster, using endothelial-specific gene sets as input (**Table S3**). Grouping by aspects (groups of similar gene sets based on gene components and cell separation across the data) allowed us to test how well different endothelial functions mapped onto our clustering (Fig. 1c; **Extended Data** Fig. 2b; **Table S4**)[25]. Second, to uncover novel active gene regulatory networks important in cellular identity and differentiation of our clusters, we employed single-cell regulatory network inference and clustering (SCENIC)[26]. We identified 167 unique regulons across the data and reveal enriched regulon activity for each cluster (Fig. 1d-e; **Extended Data** Fig. 2c-d; **Table S5**) Together these analyses uncover the full spectrum of cellular complexity within the enteric vascular bed.

As expected, post-capillary venules (PCV) were best defined by genes and pathways involved in leukocyte trafficking, whereas artery development was most evident in arteries (Fig. 1c). We also detected an artery shear stress (SS) cluster (expressing genes including *Slc6a6*, *S100a4*, *Pi16*; and enriched for *Crem* and *Klf11* regulons) previously identified only in the brain[7] (Fig. 1d-e, **Extended Data** Fig. 2a). As a group, capillary ECs were enriched for fatty acid transport and metabolism, whereas large vessel ECs together show increased oxidative phosphorylation. The major BEC population were capillary arterial cells (50%), defined by high activity of *Rara*, suggestive of a role for Vitamin A metabolite retinoic acid (RA) in enteric capillary homeostasis (Fig. 1d-e). Capillary 1 were enriched for angiogenic/tip cell genes (*Apln*, *Chrm2*, *Car4*)[5,27], proliferative and chemotaxis pathways, and *Srebf1* activity linked previously to promotion of VEGF-mediated angiogenesis[28], all in keeping with its identification as a novel gut angiogenic endothelial subset. Conversely, capillary 2 markers included *Ces2e*, *Ramp3*, *Rbp7* and presented with specific *Rarg* activity, further implicating RA in intestinal capillary identity. Capillary 3 were reminiscent of previously described Aqp7^{+}-capillaries[7], and indeed showed a preference for aquaporin-mediated water transport. Interestingly, capillary 3 shared many key regulons with PCVs, suggesting it could be a venous-end population.

Our data resolved enteric LEC into 4 novel clusters. The major components were LEC1 and LEC2a that share similar canonical LEC markers (for example *Nrp2*, *Cp*, *Mmrn1*), but were separated by enrichment for hypoxia in LEC1, and enrichment for MHC class I-mediated presentation in LEC2a (**Extended Data** Fig. 2a; Fig. 1c). We identified a clear IFN response signature in IFN LEC at marker (*Ifit1-3*, *Rsad2*, *Isg15*), aspect (IFN response) and regulon levels (*Stat1-2*, *Irf2*, *Irf7*). Intriguingly, we also detected an immunomodulatory LEC population, LEC 2b, defined by metallothionein gene expression (*Mt1*, *Mt2*), and akin to PCVs, that were enriched for leukocyte trafficking pathways with many of the same transcription factor activities, including NF-kB signalling (*Relb*, *Hivep2*; Fig. 1c)[29]. Collectively, these data deconstruct enteric endothelial heterogeneity at the level of marker, biological role, and transcription factor-driven identity.

Endothelial sensing of AHR ligands

To study the direct impact of AHR ligand sensing on ECs, we split the scRNAseq dataset into vehicle- and AHR ligand-treated conditions. As expected, acute systemic exposure (3h) to AHR ligand did not alter the relative proportions of EC subtypes (Fig. 2a, **Extended Data** Fig. 3a). We observed a striking and broad induction of AHR-specific target gene *Cyp1a1* across all EC subtypes, while *Cyp1b1*, another canonical AHR target, was significantly enriched in all clusters except Cap 3 (Fig. 2b, **Extended Data** Fig. 3b). In the absence of ligand treatment only a low proportion of cells in 3 clusters (Cap 1, LEC 1, LEC IFN) expressed *Cyp1a1*, indicative of physiological ligand sensing activity (**Extended Data** Fig. 3c). However, proportions of AHR responsive cells upon ligand exposure were similar (> 80%) in all EC subtypes (**Extended Data** Fig. 3c), suggesting sensitivity to AHR ligands is a universal feature of gut EC subtypes.

Next, we set out to verify this finding by flow cytometry using a *Cyp1a1* fate-reporter strain that reports AHR activity through induction of an enhanced yellow fluorescent protein (eYFP) activated through targeted insertion of Cre recombinase in the mouse *Cyp1a1* locus[30]. Following systemic administration of potent AHR ligand 3-methylcholanthrene (3-MC), both BEC ($CD31^{+}PDPN^{-}$) and LEC ($CD31^{+}PDPN^{+}$) populations showed AHR-responsiveness (Fig. 2c, **Extended Data** Fig. 3d). In addition, whole-mount gut imaging of ligand-treated *Cyp1a1*-reporter mice revealed AHR ligand sensing was not localised to specific intestinal segments and appeared universal throughout blood and lymphatic vessels (Fig. 2d, **Extended Data** Fig. 3e-f). This was further confirmed by flow cytometry, demonstrating no difference in *Cyp1a1*-reporter activity between duodenum, jejunum, and ileum after ligand administration (**Extended** Fig. 3g-h). Indeed, endothelial AHR responsiveness to systemic ligand was not restricted to the small intestine. BEC sensitivity was noted in colon, liver, lung, spleen, kidney, and adipose tissues; and LEC sensitivity observed in colon and liver (**Extended** Fig. 3i). Together, these data suggest that AHR responsiveness is a conserved feature of enteric ECs across vessel-types along the length of the intestine – the major source of dietary and microbial AHR ligands – but AHR signalling is also employed by ECs of other organs.

To understand the impact of AHR pathway activation within each EC subtype, we performed differential gene expression analysis between ligand and vehicle treated cells within each cluster. Alongside canonical AHR pathway genes (*Cyp1a1*, *Cyp1b1*, *Tiparp*) one main pattern emerged: consistent differentially expressed (DE) gene changes were associated with negative regulation of proliferative and angiogenic/lymphangiogenic processes, including increased *Cdkn1a* and *Zfp36l1*, and decreased *Sox18*, and *Nrp2* (Fig. 2e; **Extended Data** Fig. 4a; **Table S6**)[31–34]. BEC cluster transcriptional responses were predominantly unique to each cluster, while LEC cluster responses were more similar – predominantly unique, or shared between at least 3 clusters (**Extended Data** Fig. 4b). 12 DE genes were shared amongst all EC clusters including a shared up-regulation of anti-proliferative *Cdkn1a*, oxidative stress protector *Txnip*, and transcription factor *Klf9* - linked to quiescence in other cell types[35,36], and a shared downregulation of key endothelial motility gene *Marcks*[37]. (**Extended Data** Fig. 4c-e; **Table S7**). At the pathway level, we observed consistent downregulation of pathways related to angiogenesis, vasculogenesis, endothelial cell proliferation and endothelial cell migration amongst BEC clusters in AHR ligand-treated animals (Fig. 2f; **Extended Data** Fig. 4f; **Table S8**). Following ligand exposure, LEC clusters displayed reduced responses to TGF-b, inflammatory signalling (IL-1b, LPS), as well as a consistent

inhibition of cell migration and growth factor signalling. Combined downregulation of angiogenic, inflammatory and TGF-b pathways support the notion that AHR ligands provide important homeostatic environmental cues to ensure EC quiescence at the intestinal barrier[1].

EC-intrinsic AHR signalling regulates proliferation

In order to determine how a lack of responsiveness to AHR ligands affects intestinal EC function, we generated an inducible EC-specific *Ahr*-deficient mouse model - *Cdh5(PAC)*$^{Cre/ERT2}$*Ahr*$^{fl/f\ NuTRAP}$ (EC$^{\Delta Ahr}$)[38,39]. Following tamoxifen treatment (5x injections) in adult mice, we observed specific, and efficient Cre induction in intestinal BEC and LEC (**Extended Data Fig. 5a**), with no significant changes to the intestinal immune cell infiltrate during tamoxifen treatment (**Extended Data Fig. 5b**). To understand EC-specific transcriptomic changes, we administered EC$^{\Delta Ahr}$ and AHR WT (EC^{WT}) control mice with short-term FICZ treatment (3h) before sorting and sequencing SI BEC and LEC (**Extended Data Fig. 5c**). *Ahr*-deficient BEC displayed differential expression of 664 genes, including a prominent downregulation of AHR target genes (*Cyp1a1, Cyp1b1, Tiparp, Nqo1, Ahrr*) indicative of a lack of responsiveness to AHR ligand stimulation as a consequence of successful *Ahr* deletion in these mice (Fig. 3a; **Table S9**). *Ahr*-deficient BEC showed marked enrichment for pathways relating to inflammatory response, mesenchymal transition, angiogenesis, cell motility, and leukocyte recruitment (Fig. 3b-c; **Table S10**). 1215 DE genes were found between EC$^{\Delta Ahr}$ LEC and their EC^{WT} LEC counterparts (15% of which are shared with BEC DE genes), with enrichments in oxidative phosphorylation, ROS, Myc targets, and mesenchymal transition (**Extended Data Fig. 5d-f**). Combined, this data illustrates AHR as a key component of endothelial cell quiescence – regulating both angiogenic and inflammatory activation processes in tandem.

Based on these data, we hypothesised that AHR-deficient endothelial cells should display altered proliferative regulation *in vivo*. We used a single dose of tamoxifen to suboptimally delete *Ahr* in EC$^{\Delta Ahr}$ mice, and made use of Cre-induced fluorescent tagging within this model to compare AHR-sufficient (eGFP^{-}) with AHR-deficient (eGFP^{+}) ECs within the same animals. To analyse proliferation, we subjected mice to *in vivo* 5-Ethynyl-2'-deoxyuridine (EdU) labelling over 2 weeks. The majority of endothelial cells exist in a state of functional quiescence at homeostasis, but signals actively promoting this remain ill-defined[1]. We were able to demonstrate a small but significant increase in endothelial cell proliferation during this period in both enteric BEC and LEC in the absence of AHR ligand sensing (Fig. 3d). Given the dependence of gut vascular endothelium on vascular endothelial growth factor A (VEGFA) for physiologic angiogenesis and optimal maintenance of the enteric vascular bed[40,41],we also tested proliferation in AHR-deficient ECs in mice treated with recombinant VEGFA$_{165}$ alongside EdU treatment for 2 weeks. Surprisingly, even with the addition of this potent EC mitogen, *Ahr*-deficient BEC were still imbued with a higher proliferative capacity than *Ahr*-sufficient BEC (Fig. 3e), demonstrating the importance of AHR in promoting enteric EC proliferative restraint during homeostasis. These data combined support the view of AHR as a proliferative rheostat in the gut for blood EC homeostasis.

We next examined the impact of EC AHR-deficiency at whole tissue level. At homeostasis, gut immune cell composition was unaltered between $EC^{\Delta Ahr}$ and EC^{WT} mice (**Extended Data Fig. 6a-b**). Similarly, there were no changes in the inflammatory activation profile of intestinal epithelial cells (IECs) as assessed by MHC-II, ICAM-1 and CD74 expression[42–44] (**Extended Data Fig. 6c**). Additionally, to examine transcriptomic changes at whole tissue level, we performed whole-tissue RNAseq on small intestine from $EC^{\Delta Ahr}$ and EC^{WT} mice following a 3h FICZ treatment, finding very few differences between the groups (12 DE genes total; **Extended Data Fig. 6d-e**). To examine morphological and angiogenic changes to the intestinal vascular landscape in $EC^{\Delta Ahr}$ mice, we employed whole mount imaging approaches. $EC^{\Delta Ahr}$ and EC^{WT} mice were treated with tamoxifen (5x injections), followed by 3-MC 1 week prior to tissue collection (Fig. 3f). Over the timeframe analysed, endothelial AHR signalling did not impact villi blood vascular density or branching, villus vascular cage height, or lacteal length (**Extended Data Fig. 6f**). To study intestinal vascular integrity, we again treated mice with 3-MC for 1 week before injecting 100nm fluorescent microspheres intravenously and analysed their tissue dissemination after 5 minutes circulation time[45]. As previously reported, substantial leakage was seen from MADCAM-1^+ submucosal venules with minimal leakage in villi or crypt vasculture[46], but this did not differ between the two groups within any vessel (**Extended Data Fig. 6g**). However, in agreement with *in vivo* proliferation detected by EdU incorporation (Fig. 3d-e), and tissue-wide RNAseq enrichment of *Esm1* (**Extended Data Fig. 6d-e**), expression of tip cell marker and VEGFA target ESM1 was enriched in $EC^{\Delta Ahr}$ mice (Fig. 3f)[46]. Together, these data suggest that endothelial AHR activation in the adult gut at homeostasis primarily functions to limit endothelial proliferation and angiogenesis[47].

Endothelial AHR restrains EC inflammatory activation

Next, to understand how dietary AHR ligands influence endothelial cell-intrinsic responses to inflammation, $EC^{\Delta Ahr}$ mice were first fed *ad libitum* with diet containing AHR pro-ligand indole-3-carbinol (I3C), a vegetable-derived phytochemical converted to high-affinity AHR ligands DIM and ICZ by exposure to stomach acid. After a week of dietary intervention, mice were challenged with lipopolysaccharide (LPS), or vehicle (PBS). Using suboptimal *Ahr*-depletion, we observed that compared to WT BEC, KO BEC within LPS-treated $EC^{\Delta Ahr}$ mice demonstrated increased expression of inflammatory markers ICAM-1, VCAM-1, PD-L1, and BST2; fatty acid transporter and pro-inflammatory mediator CD36; and proliferative markers CD105 and CD24 (**Extended Data Fig. 7a**)[48–50]. When assessing costimulatory molecules CD80 and CD86, we noted CD80 was very lowly expressed in BEC, but expression of CD86 was clear and enhanced in AHR-deficient ECs following LPS treatment (**Extended Data Fig. 7a**). Notably, inflammatory challenge was required to reveal these AHR-linked expression changes, as in vehicle-treated mice BST2, CD86, and CD105 were the only gut EC activation markers (those that were expressed higher upon LPS treatment) increased in AHR-deficient ECs (**Extended Data Fig. 7a**). CD24 and CD36 expression increases in KO BEC were consistent in both PBS and LPS treatment. Similarly, in LEC, LPS treatment was required to reveal the full extent of these expression changes, with enhanced expression of ICAM-1, VCAM-1, MHC-II and BST2, but PD-L1 repressed in KO LEC (**Extended Data Fig. 7b**). Strikingly, endothelial AHR-deficiency promoted large increases in the expression of key endothelial cell inflammatory makers (ICAM-

1, VCAM-1 for BEC; MHC-II for LEC) akin to those induced by LPS, demonstrating the anti-inflammatory potency of AHR signalling in ECs.

Finally, to determine whether endothelial AHR influences the outcome of enteric infection, we used the enteric pathogen *Yersinia pseudotuberculosis* (*Yptb*). Infection with the extracellular gram-negative pathogen *Yptb* causes acute gastroenteritis, mesenteric lymphadenitis and diarrheal disease in both humans and mice[51]. *Yptb* rapidly disseminate through the intestinal lamina propria and gut draining mesenteric lymph nodes (mLN), before reaching spleen and liver via both the enteric blood and lymphatic vasculature[52]. Our data demonstrate for the first time that mice with germline deficiency in *Ahr* are highly susceptible to *Yptb* infection, with dramatically reduced survival and increased bacterial load in peripheral organs compared to WT mice (**Extended Data Fig. 8a-c).** To test whether AHR-mediated protection against *Yptb* depends on dietary ligands, we infected mice fed either a purified diet (low in AHR ligands, PD), or I3C-containing diet (high in AHR ligands, I3C). Removal of dietary AHR ligands in WT mice led to reduced survival after *Yptb* infection, compared to mice fed I3C supplemented diet (Fig. 3g), demonstrating a non-redundant role for nutritional AHR ligands in conferring protection to *Yptb*.

To determine whether dietary AHR ligands mediate these protective effects through ECs, we infected $EC^{\Delta Ahr}$ and EC^{WT} mice on I3C diet with *Yptb*. Our data suggest endothelial AHR partially contributes to protection from *Yptb* infection, with statistical significance reached in female mice (survival: males - EC^{WT} 83% $EC^{\Delta Ahr}$ 64%; females - EC^{WT} 79% $EC^{\Delta Ahr}$ 45%; Fig. 3h). Unlike in the global $Ahr^{-/-}$ mice, there were no clear differences in bacterial dissemination to the spleen or liver, and no difference in the bacterial load in Peyer's patches (PP) (Fig. 3i); suggestive of a role for vascular AHR in promoting disease tolerance rather than gut vascular barrier integrity or direct anti-bacterial immunity[53,54]. Accordingly, $EC^{\Delta Ahr}$ displayed a dysregulated immune infiltrate in the gut lamina propria 3-days after *Yptb* infection. We observed increased eosinophil, dendritic cell, NK cell, and γð T cell abundance in the SI, whereas numbers of resident populations (macrophages) and adaptive immune cells involved at later timepoints (B cells, $CD4^+$ T cells, $CD8^+$ T cells) remained unchanged. (Fig. 3j, **Extended Data Fig. 8d)**. Together, our data suggest a role for endothelial AHR in promoting disease tolerance to enteric infection through modulating intestinal immune composition to limit inflammation.

AHR ligands maintain vascular normalcy in human ECs

So far, our findings demonstrate that AHR ligands serve as important environmental cues for maintenance of functionally quiescent ECs in mice. To ascertain whether AHR ligands impart similar vasculoprotective programs in human ECs, we cultured primary human umbilical vein endothelial cells (HUVECs) with or without AHR ligand FICZ. Exposure of HUVECs to FICZ led to transient AHR pathway activation (**Extended Data Fig. 9a)** and RNAseq revealed the full spectrum of AHR-regulated genes in HUVECs (Fig. 4a; **Table S11**). HUVECs are highly proliferative cells in culture but quiescence can be induced under certain conditions *in vitro*[55]. Based on a published RNA-seq dataset of proliferating and quiescent HUVECs, we generated custom genesets to interrogate whether AHR pathway activation can

regulate these specific cellular states in human ECs[55]. AHR ligand exposure promoted transcriptional signatures associated with EC quiescence while inhibiting cell proliferation (Fig. 4b). Further assessment of EC proliferation by flow cytometry revealed an increase in the frequency of cells in G0/G1, and a corresponding decrease of cells in S phase upon short-term (6h) exposure (Fig. 4c). Conversely, *AHR* knockdown in HUVECs had the opposite effect, with fewer cells in G0/G1, and more in S phase (**Extended Data Fig. 9b**). To determine whether this cell cycle inhibition was due to altered expression of prototypic cell cycle regulators, we performed quantitative single-cell immunofluorescence. Following FICZ stimulation, we observed a decreased fraction of cells in S-phase (Edu^+) in concert with decreased protein expression of E2F, a cell cycle transcription factor, decreased Rb phosphorylation (pRb) and increased expression of the cell cycle inhibitor, p27 (Fig. 4d-e, **Extended Data Fig. 9c**).

Functionally quiescent ECs retain the ability to undergo rapid activation in response to inflammatory mediators such as LPS. Accordingly, stimulation of HUVECs with LPS induced expression of an array of adhesion molecules and pro-inflammatory cytokines and chemokines. This LPS-induced inflammatory response was significantly dampened in the presence of FICZ, demonstrating the potent anti-inflammatory potential of AHR ligands (Fig. 4f). Together, our data in human ECs are consistent with those seen in mice, lending further support to the conserved role of AHR ligands as important environmental cues for the maintenance of endothelial quiescence.

Discussion

Activation of the blood and lymphatic vasculature that supply and drain the gut must be tightly regulated to preserve tissue homeostasis and prevent aberrant inflammatory responses. In this study we demonstrate that the AHR provides a direct functional link between nutritional signals and the active maintenance of endothelial quiescence in mice and humans.

First, we uncovered the full cellular complexity of the murine small intestinal endothelial compartment at single-cell resolution. While a recently published single-cell endothelial atlas made great strides in understanding inter-organ endothelial diversity in mice, the small intestinal EC compartment was underrepresented in that dataset[7]. Our study specifically focused on this important barrier surface, revealing the full spectrum of EC heterogeneity. Newly identified features include the 4 distinct LEC subtypes, emergence of a novel angiogenic capillary population, and a shear stress-related artery cluster. Our detailed analyses facilitated the identification of biological roles for these newly described subsets. For example, we discovered two LEC capillary subtypes exhibiting immunomodulatory features. PCV-like LEC2b that could play a role in immune cell migration; and IFN-responsive LEC - similar to a LEC subtype recently identified in mesenteric adipose[6] - that may participate in the maintenance of intestinal immune homeostasis through integration of microbiota-driven tonic IFN signalling. We additionally identified a pro-angiogenic capillary subtype (capillary 1) within the intestine. This cluster shares features with angiogenic ECs identified in multiple other organs[7], capillary precursor BEC identified in murine lymph nodes[5], and retinal-tip like *Car4*$^+$ BEC described in murine lung[27]. The position of these cells within the

vascular network, and their specific involvement in homeostatic and pathogenic angiogenesis is the subject of further study. Moreover, we identified a plethora of EC subtype-specific transcriptional regulons – programs that shape cellular identity and will advance understanding of enteric EC heterogeneity. Among these findings, we suggest the importance of Vitamin A metabolites in gut capillary transcriptional regulation and function, through predominant *Rara* and *Rarg* activity in capillary arterial and capillary 2 populations respectively. RA has a well-known role in vascular development and is also a potent inducer of the blood brain barrier (BBB) phenotype in mice and human ECs[56]. Based on this, our data suggest a role for the dietary micronutrient Vitamin A and its metabolites in the control of gut-vascular barrier integrity[54]. The *Foxp4* regulon was found to be central to immunoregulatory LEC2b identity, with roles only previously ascribed to gut epithelial, and immune populations[57,58]. Interestingly canonical venous transcription factor *Nr2f2* activity was much more focused in the LEC supercluster than PCVs in the intestine[41]. Furthermore, while certain transcription factor families are well known for their importance in endothelial biology (KLF, SOX)[34,59], we reveal specific members such as *Klf10* and *Sox7* to be implicated in subset-specific control for the first time. Future work will investigate how these different EC subtypes communicate, cooperate, and respond to homeostatic perturbations.

Interestingly, despite the substantial small intestinal EC heterogeneity we revealed responsiveness to AHR ligand stimulation was a universal feature of ECs, highlighting the role of this environmental sensor as a key facet of gut EC biology. At steady state, endothelial AHR sensing in the adult gut was not responsible for controlling vascular morphology and integrity, nor did it have an EC-intrinsic role in controlling epithelial activation or immune system recruitment. However, AHR ligand sensing was crucial in the promotion of several aspects of functional EC quiescence: an active process that requires coordinated suppression of proliferative, migratory, and inflammatory programs necessary for the maintenance of vascular normalcy and organ homeostasis[1,60].

First, AHR activation suppressed endothelial proliferation. This is highly consistent throughout our transcriptomic (Fig. 2c,f; Fig. 3a-c; Fig. 4a-b; Extended Data Figs. 4a,f; 5d-e) and functional data (Fig. 3d-f; Fig. 4c-e; Extended Data Fig. 9) in mice and human cells and supported by previous *in vitro* studies[23,61]. While the majority of EC *in vivo* are maintained in quiescence, some ECs undergo homeostatic proliferation in non-pathogenic angiogenesis. In particular, lymphatic lacteal LEC proliferate more than EC from other beds to maintain this vascular niche[62,63]. Notably, we show that AHR signalling limits the proliferation of such ECs, an important checkpoint in preventing aberrant angiogenesis. Furthermore, AHR signalling can dampen the responses to the potent EC mitogen VEGFA, as evidenced by increased proliferation in $EC^{\Delta Ahr}$ mice in response to exogenous VEGF, and increased active VEGFA signalling in the villi vasculature of these mice as shown by elevated ESM1 protein levels[47]. This is particularly interesting given the reliance of the intestinal vasculature and other fenestrated beds on continuous low level VEGFA signalling for endothelial maintenance[1,40,64]. However, given that we saw no differences in intestinal vascular morphology or leakage in $EC^{\Delta Ahr}$ mice, we propose that AHR fine-tunes the VEGFA response, acting primarily to restrain excess proliferation, without leading to a loss of endothelial identity in the gut. Given the clear function of the AHR as an anti-proliferative mediator in the adult vasculature, and known

AHR involvement in non-specific vascular development[17], determining the role of AHR-mediated ligand sensing in enteric vasculature development and postnatally before adulthood remain interesting research questions.

Second, AHR ligand sensing in ECs acts as a potent anti-inflammatory signal. Exposure to AHR ligands dampened inflammatory activation following LPS challenge *in vivo* and *in vitro* in our study, through downmodulation of adhesion molecules, cytokines, and chemokines. AHR is known to negatively regulate type 1 IFN and NFkB signalling pathways,[65,66] and global *Ahr*-deficiency is associated with heightened susceptibility to endotoxemia[67]. Further, endothelial AHR-mediated dietary ligand sensing was required for optimal responses to enteric infection. There was a significant impact on survival in female $EC^{\Delta Ahr}$ mice, and the small intestines of $EC^{\Delta Ahr}$ mice contained more eosinophils, DCs, NK cells and γδ-T cells that together suggest key perturbations in the composition of the inflammatory milieu at early stages of infection. ECs express a range of innate immune receptors, and can integrate signals from immune cells, as well as secrete pro-inflammatory mediators to modulate immunity[68]. Sensing of dietary AHR ligands may therefore provide a way to restrain endothelial activation, and avert sustained inflammatory responses to enteric pathogens, analogous to the role of AHR in promoting disease tolerance following lung infection described in the accompanying manuscript (Major et al.). This role of AHR in gut ECs adds a new dimension to the holistic dependence of the intestine on AHR for optimum enteric immunity, adding an endothelial component to the described roles of epithelial cells and immune populations[12,13,15]. How the AHR pathway integrates with other known regulators of endothelial quiescence such as ERG[69,70], or metabolic quiescence regulator FOXO1[71] requires further study. AHR activation in intestinal epithelial and immune cells has been shown to mediate tissue-protective responses[9], and our data presented here identifies endothelial-intrinsic programs necessary for intestinal homeostasis. It is now becoming increasingly recognised that ECs provide a nurturing niche for tissue-resident stem cells, participate in host-defence against pathogens and orchestrate tissue regeneration upon injury in various organs[72]. Our study further adds to the recent identification of molecular determinants of enteric EC survival, demonstrating that AHR ligand sensing is a key controller of enteric EC proliferative and inflammatory quiescence, with a picture emerging of enteric EC as an important contributor to gut homeostasis[60,73].

Lastly, our data also show that EC responsiveness to nutritional AHR ligands may extend to other organs, potentially impacting EC quiescence and function systemically. The intestinal lumen is a rich source of AHR ligands, which not only act locally within the intestinal compartment but can reach distal organs via the vasculature[74]. Sensing of gut-derived AHR ligands within the intestine can be described as ‘outside-in’ with epithelial cells as frontline responders followed by immune and structural cells, including ECs. However, in organs other than the intestine, ECs represent the main portal of entry for gut-derived AHR ligands into the tissue parenchyma, representing an 'inside-out’ route of ligand exposure. How these two scenarios differ in terms of relative contribution of AHR-responsive cell-types to organ homeostasis and integration of environmental cues derived from the gut-axis requires further study. The accompanying

paper by Major *et al* dissects the function of AHR in lung ECs and reveals a role of 'inside-out' ligand exposure along the gut-lung axis for protection from virus-induced lung damage.

In sum, our study sheds light on intestinal adaptations to environmental cues, demonstrating that endothelial AHR ligand sensing acts as a crucial node for the maintenance of vascular normalcy across EC subtypes. With endothelial dysfunction increasingly recognised as a hallmark of chronic inflammatory disease, our data points towards a potential role for AHR activation through dietary ligand supplementation as a therapeutic strategy to facilitate organ homeostasis and disease resilience.

Methods

Mouse models:

Cdh5(PAC)$^{Cre/ERT2}$*Ahr*$^{fl/f}$, *Cdh5(PAC)*$^{Cre/ERT2}$*Ahr*$^{fl/f\ NuTRAP}$, *Cyp1a1*^{Cre}*R26*$^{LSL-eYFP}$, and *Ahr*$^{-/-}$ mice were bred and maintained at the Imperial College London Central Biological Services facility. Wild-type mice used in scRNAseq experiments were purchased from Charles River, UK. All mice were on a C57BL/6 background. Mice were bred and maintained in individually ventilated cages under specific-pathogen free conditions according to UK Home Office and local ethics committee (AWERB) approval. Cage and age-matched littermates served as experimental controls. Mice were between 6–16 weeks at time of experiments, and male mice used throughout, except infection studies where a mixture of male and female mice were used. scRNAseq – 3 mice/group, RNAseq – 2–3 mice/group used to obtain required cell frequencies.

In vivo interventions:

Tamoxifen

Mice were dosed with tamoxifen i.p. (100mg/kg in corn oil) either once, or every other day for 14 days at 5–8 weeks of age[75].

AHR ligand administration

6-Formylindolo(3,2-b)carbazole (FICZ; Sigma, UK) was prepared to 20mg/ml in DMSO and diluted to 2mg/ml working stock in corn oil in glass containers. 3-Methylcholanthrene (3-MC; Sigma, UK) was prepared in corn oil to 5.3mgml. FICZ and 3-MC were then injected i.p at 5ml/g – 10mg/kg and 26.5mg/kg respectively. For dietary interventions, mice were fed either a purified diet, or a purified diet supplemented with 1000mg/kg indole-3-carbinol (I3C) (both Ssniff, Germany) *ad libitum* for 8 days.

LPS treatment

Lipopolysaccharide (LPS; Sigma, UK) was given i.p. at 10mg/kg in sterile PBS for 24h.

EdU feeding: 5-ethynyl-2'-deoxyuridine (EdU; Thermo Fisher, UK) was first dissolved in DMSO to 50mg/ml and then further diluted to working dilution to be given to mice at 30mg/kg i.p. (30mg/kg) on day 0. EdU

was added to the drinking water at 0.3mg/ml of drinking water as previously described[76]. Edu-water was replaced fresh every 2–3 days.

VEGFA administration

Murine $VEGFA_{165}$ (Peprotech) stock was made in 100mg/ml in sterile PBS and administered intraperitoneally at 5mg/mouse in sterile PBS bi-weekly over 2 week EdU-feeding period (4x doses).

Administration of 100nm microspheres

100nm fluorescent microspheres (580/605 FluoSpheres, Thermo Fisher) were vortexed thoroughly, diluted 1/5 in sterile PBS and administered intravenously at 100ml/mouse. SI tissues were taken for whole mount imaging analysis after 5 minutes as previously described[46].

Yersinia pseudotuberculosis infection: *Yersinia pseudotuberculosis* (32777) was grown (27°C, 300rpm) overnight in 2xYT media supplemented with 2µg/ml Irgasan (Sigma, UK). Mice were infected by bacterial solution washed twice and resuspended in PBS (200ml/mouse – 5×10^7 or 5×10^8 CFU as described).

Tissue digestion

Following harvesting and fat removal, small intestine (SI) and colon were cut open longitudinally, and underwent an IEL wash: incubated with IEL wash buffer (IMDM + 1%FCS, 5 mM EDTA, 10 mM HEPES, penicillin/streptomycin, and 2 mM DTT) for 20 min at 37°C with 200rpm. shaking. Small intestine was washed and vortexed at low speeds in SI PBS (PBS + 5mM EDTA + 10mM HEPES) 30seconds x 3 times or until clear, and then vortexed at low speed in PBS. Colon was vortexed in PBS once. Both gut tissues were then cut into small pieces and incubated in digestion buffer. All other tissues (BAT, iWAT, liver, lung, kidney spleen) were cut into small pieces and incubated directly in digestion buffer.

For EC-tailored digests, all organs were digested by incubation in Collagenase A digestion buffer (4mls/tissue: HBSS + 20mM HEPES, 10mg/ml Collagenase A (Sigma), 8U/ml Dispase II (Sigma), 50mg/ml DNase I (Sigma) for 20 minutes at 37°C with 200rpm shaking. For immune cell digests, organs were incubated in Collagenase VIII digestion buffer (5mls/tissue: IMDM + 1% FBS, 10nM HEPES, penicillin/streptomycin, 1mg/ml Collageanse VIII (Sigma), 50mg/ml DNase I. All reactions stopped through addition of 1:1 complete media (IMDM + 1%FCS, penicillin/streptomycin, 1x glutamax) and: passing through 100mm filters (SI, colon, kidney, lung, spleen); debris removal through 2x 1minute 60g centrifugation, harvesting supernatant and then passing through 100mm filters (liver); or 250g 10-minute centrifugation and careful floating adipocyte fraction removal (BAT, iWAT). After centrifugation (400g, 8 minutes), SI and colon were subjected to 40% Percoll (Amersham) density gradient centrifugation (400g, 8 minutes) to remove debris, while all other tissues underwent resuspension in 0.5ml ACK lysis buffer for 2 minutes and washing to remove erythrocytes. Finally, cells were filtered (40mm) and counted before downstream analysis.

Primary cell culture

Primary human umbilical vein endothelial cells (HUVEC; Lonza, UK) obtained from pooled donors were seeded at 60–80% confluency and cultured in Endothelial Cell Growth Medium-2 media (EGM-2 Bulletkit; Lonza) supplemented with penicillin/streptomycin(P/S) at 5% CO_2 and 37^{o}C. Cells were switched to minimal growth media (EGM-2 Bullet kit basal medium, Lonza; supplemented with P/S) for 24h prior to experimentation. For FICZ stimulation experiments, FICZ (between 0.1-100nM), or DMSO control were added to the cells for indicated time points. For LPS/FICZ dual stimulation experiments, cells were treated with (a) DMSO only (1:1000, Fisher Scientific, UK), (b) LPS only (50 ng/ml final concentration, InvivoGen), (c) FICZ only (100nM final concentration, Enzo) or (d) FICZ/LPS for 6h in total. Fresh DMSO, LPS and FICZ were added to (a), (b) and (c) after 2h, respectively. FICZ/LPS group was treated with FICZ for 2h initially followed by stimulation with FICZ and LPS for 6h. HUVECs between passage 1 and 4 were used in experiments.

Transfection

HUVECs were grown to 60–80% confluency, before addition of 1µg of ON-TARGETplus Human AHR (196) siRNA – SMART pool (SiScr) (Horizon, L-004990-00-0050) or 1µg ON-TARGET plus Non-Targeting Pool (SiScr) (Horizon, D-001810-10-50) for 24h. Media was changed 1 hour prior to transfection.

Quantitative real-time PCR

RNA was purified from frozen HUVEC using TRIzol Plus RNA Purification Kit (ThermoFisher), or using RNeasy Plus micro kit (Qiagen) for FICZ/LPS treated HUVEC experiments. cDNA was generated using High Capacity cDNA reverse transcription kit (ThermoFisher). qPCR was performed with Sso advanced universal SYBR Green Supermix (Biorad) using the following primers:

- *AHR*: forward 5’ GCCCTTCCCGCAAGATGTTAT 3’; reverse 5’ CAAAGCCATTCAGAGCCTGT 3’
- *CYP1A1*: forward 5’ CAATGAGTTTGGGGAGGTTACTG 3’; reverse 5’ CAATTCGGATCTGCAGCACG 3’
- *CCL2*: forward 5’ AGACTAACCCAGAAACATCC 3’; reverse 5’ ATTGATTGCATCTGGCTG 3’
- *CXCL6*: forward 5’ CCTCTCTTGACCACTATGAG 3’; reverse 5’ GTTTGGGGTTTACTCTCAG 3’
- *IL*6: forward 5’ GCAGAAAAAGGCAAAGAAT 3’; reverse 5’ CTACATTTGCCGAAGAGC 3’
- *IL8*: forward 5’ GTTTTTGAAGAGGGCTGAG 3’; reverse 5’ TTTGCTTGAAGTTTCACTGG 3’
- *SELE*: forward 5’ GAGAATTCACCTACAAGTCC 3’; reverse 5’ AGGCTTGAACATTTTACCAC 3’
- *ICAM1*: forward 5’ ACCATCTACAGCTTTCCG3’; reverse 3’ TCACACTTCACTGTCACC5’

Flow cytometry and FACS

For mouse experiments, cell suspensions were incubated with anti-mouse CD16/CD32 (TrustainFx, Biolegend), before incubation with live/dead dye (zombie near infra-red, Biolegend), and incubation with surface antibodies (See Table S12). All antibodies and subsequent washes in FACS buffer (PBS + 2% FCS, 2mM EDTA). For EdU detection, Click-iT EdU proliferation kit – pacific blue (ThermoFisher) was used, according to manufacturer’s instructions. DAPI nuclear stain added directly < 5minutes prior to analysis/sorting. A combination of compensation beads (OneComp/Ultracomp eBeads, ThermoFisher)

for antibody controls, and single-stained cells for dyes and fluorescent proteins were used for controls and for compensation/spectral unmixing.

For HUVEC proliferation experiments, Click-iT EdU proliferation kit AlexaFluor647 was used according to manufacturer's instructions. Briefly, this involved a 1h EdU pulse to cells prior to washing, fixing, DAPI staining, and analysis.

Samples were run on a LSR II flow cytometer running FACSDiva software (BD), a Cytek Aurora spectral cytometer running Spectoflo software (Cytek); or sorted on an Aria Fusion with FACSDiva (BD). Data analysed offline using FlowJo v10 (BD). Multi-immune cell gating based on refs [77,78].

For single-cell RNAseq experiments, total live endothelial cells were FACS sorted (80mm nozzle size, < 5.0 flow rate) into collection buffer (PBS + 10%FCS), counted manually, and taken forward to single-cell barcoding in PBS + 0.04% BSA. For mouse RNAseq experiments cells were FACS sorted (settings as above) into RLT buffer (Qiagen) containing 1% b-mercaptoethanol (Sigma) and placed immediately onto dry ice before RNA isolation.

Single-cell RNA sequencing

scRNAseq

Sorted mouse $CD31^{+}CD45^{-}$ single-cell suspensions (viability > 80%) were obtained from three samples across two conditions (1 vehicle-treated, 2 FICZ-treated) aiming for 15,000 cells per library and a sequencing depth of 50,000 reads per cell. Both FICZ-treated samples were from the same pool of cells, used in the experiment to match cell numbers with the vehicle sample. Cells were partitioned using the 10X chromium controller and the resulting GEMs (Gel bead in Emulsion) were converted into scRNA-seq libraries using the 10x Single Cell 3' v3 kit according to manufacturer specifications. Libraries were sequenced on an Illumina 2500 generating Paired-End 100bp reads which were processed using the 10x Genomic Cell Ranger pipeline v4.0.0.

Data preprocessing and QC: scRNA-seq sequencing from 3 samples (Ficz_15k, Veh_15k, Ficz_60k) was generated by Hiseq2500. Demultiplexing was performed with CellRanger (v.4.0.0; Zheng et al., 2017) mkfastq using bcl2fastq v2.17.1.14 based on the 10x library indices (allowing 0 mismatches). CellRanger count pipeline was used to perform alignment against mouse genome mm10 (using STAR), filtering, barcode counting and unique molecular identifiers (UMIs) counting. UMI count matrices were then imported to Seurat (v3.2.0)[79] with the following arguments: min.cells = 10 and min.features = 100. We further filtered cells based on the commonly used QC metrics suggested by ref [80] with the following thresholds: percentage of mitochondrial counts (per.mt) < 6%; total number of molecules detected within a cell (nCount_RNA) between 500–8000 for Ficz_60K and nCount_RNA between 500 -15000 for Ficz_15k and Veh_15k. After data preprocessing, SCTransform normalization was performed[81]. Linear dimensional reduction was performed using Seurat RunPCA() with argument npcs = 30, RunUMAP(), FindNeighbors() and FindClusters() with argument resolution = 0.5. Cells subsequently identified as doublets by

DoubletFinder[82] with parameters pN = 0.25, pk = 0.16 for Veh_15k, 0.22 for Ficz_15k and Ficz_60k were removed and the remaining cells were processed with Seurat SCTransform again and samples from Ficz and Veh were integrated using PrepSCTIntegration(), FindIntegrationAnchors() and IntegrateData() functions and the linear dimensional reduction with Seurat as described above. Both FICZ samples were integrated to form a single sample before integration with the vehicle sample for condition-wise comparisons. Cells in cluster 8, 12, 13, 14 were identified as contaminant clusters and were removed after visualisation with FeaturePlot() and VlnPlot() functions.

Clustering analysis and conserved markers

The “clean” dataset were processed with the Seurat pipeline mentioned above and in the FindClusters(), using argument resolution = 0.4. Conserved makers were further defined using the FindConservedMarkers() function from Seurat.

DE gene and pathway analysis

DE analysis for the scRNAseq was performed by using FindMarkers() function from Seurat to define genes that are differentially expressed between stimulated and control clusters. Gene set analysis on these separate lists of up-, and down-regulated DE genes was performed using EnrichR[83].

Sub-clustering and overdispersion analysis with Pagoda2

Based on the “clean” dataset, 11 clusters were identified by under resolution = 0.4. Cluster 2, cluster 3, cluster 5, cluster 6, cluster 8, cluster 9, and cluster 10 were classified as BECs and cluster 0, cluster 1, cluster 4 and cluster 7 were classified as LECs. Sub-clustering analysis was performed on BECs and LECs respectively using the SCTransform() for data normalization and PrepSCTIntegration(), FindIntegrationAnchors() and IntegrateData() functions for data integration. The linear dimensional reduction with Seurat was performed as described above but with resolution = 0.2 for both BECs and LECs.

Functional analysis for the Vehicle dataset for BECs and LECs was performed by pagoda2 (version 2_1.0.8; Fan et al., 2016, Barkas et al., 2021), using curated endothelial-related pathways (built on from ref [7] (see **Table S3**) and genesets obtained via the msigdbr() function from the R Bioconductor package msigdbr (v. 7.4.1) for MSigDB Collections C2, C5 and C7. Raw counts from BECs and LECs were imported to pagoda2[25] using basicP2proc() function for data processing with arguments “n.cores = 4, min.cells.per.gene = 10, n.odgenes = 2e3, get.largevis = FALSE, make.geneknn = FALSE”, then followed by makeKnnGraph(), getKnnClusters(), and getEmbedding(), getKnnClusters(), getDifferentialGenes() functions. Pathway overdispersion was estimated via pagoda2 with argument “correlation.distance.threshold = 0.8”.

Transcription Factor Regulon analysis with SCENIC: SCENIC version 1.2.4[84] for regulatory network analysis was performed for the scRNAseq Vehicle dataset. The workflow started from identifying

potential gene regulatory network (GRN) by using runGenie3() and runSCENIC_1_coexNetwork2modules() functions then followed by selecting potential regulons with runSCENIC_2_createRegulons() function after applying mm10__refseq-r80__500bp_up_and_100bp_down_tss.mc9nr.feather motif dataset retrieved from cisTarget databases (https://resources.aertslab.org/cistarget/). The final step was to score the regulons in the cells using runSCENIC_3_scoreCells() function. Regulon specificity scores for each cell clusters were calculated using calcRSS () function[85]. The final list of 167 regulons excluded non '_extended' duplicates when '_extended' versions were present.

ScRNAseq data visualisation

Dotplots were created by R package ggplot2. Heatmaps were created by using R Bioconductor package ComplexHeatmap[86]. Featureplots and violin plots were created by using function FeaturePlot() and VlnPlot() functions from the R Seurat package.

Bulk RNAseq analysis

RNA from FACS-sorted BEC and LEC from EC^{WT} and $EC^{D\mathit{Ahr}}$ mice (n = 3/group) was extracted with the RNeasy plus micro kit (Qiagen). RNA-seq libraries were prepared with the NEBNext Single Cell/Low Input RNA Library Prep Kit for Illumina (NEB) from 1ng total RNA., a Sequencing was then carried out with NextSeq500 using paired end 40bp reads. Illumina RTA (version 2.11.3) software and bcl2fastq (2_2.20.0) were used for basecalling and demultiplexing (allowing 0 mismatches). Raw RNAseq reads were aligned against mm10 and transcript annotations using STAR[87]. Data normalization was performed using the DESeq2 Bioconductor package[88] and was rlog transformed to allow for visualisation by PCA and heatmaps. Unwanted batch effects were controlled by using R Bioconductor package RUVseq[89] with RUVg function and k = 2. A ranked differentially expressed gene list was generated based on Wald statistics from DESeq2 results, and Gene-set enrichment analysis (GSEA) was performed using hallmark gene sets[90,91]. EnrichR was applied on separate positive and negatively enriched lists.

For mouse whole tissue RNA sequencing, pieces of small intestine were taken, washed briefly in PBS and snap frozen in liquid nitrogen. Tissue pieces were prepared using the TRIzol plus RNA purification kit (Thermo Fisher) according to manufacturer's instructions, and RNA-seq libraries prepared using NextSeq2000 using paired-end 36bp reads to achieve ~ 120M reads per sample. Reads were aligned against mouse genome GRCm38 using STAR 2.7.7a. Data normalization was performed using the DESeq2 Bioconductor package[88] and was rlog transformed to allow for visualisation by PCA and heatmapsA ranked differentially expressed gene list was generated based on Wald statistics from DESeq2 results.

For human data, HUVECs were treated with 100nM FICZ or DMSO control, for 6 hours, processed to RNA using the TRIzol Plus RNA Purification Kit as described above, and RNA-seq libraries prepared using NextSeq500 using paired-end 40bp reads to achieve ~ 40M reads per sample. Reads were aligned to Ensembl human genome (GRCh37) using tophat2 version 2.0.11[92]. Mapped reads that fell on genes were

counted using featureCounts from Rsubread package[93]. Generated count data were then used to normalise and identify differentially expressed genes using DESeq2 and DEGs were defined with Benjamini-Hochberg adjusted $P < 0.05$. Gene Set Enrichment Analysis was performed using GSEA on pre-ranked lists generated by the DESeq2 package.

Whole-mount gut imaging

Whole-mount gut imaging adapted from Bernier-Latmani et al.[94]. Briefly, small intestines were removed, the mesenteric fat cleaned, divided into duodenum, jejenum and ileum pieces, opened longitudinally and gut contents carefully cleaned in ice-cold PBS. Tissue underwent 20min intraepithelial lymphocyte wash at 37°C, 200rpm as described above. Supernatant was poured through strainer and washed in SI PBS thrice (to facilitate epithelial cell removal), then PBS once (as above) before tissue pieces pinned at 0.5cm intervals to silicone plates containing ice-cold PBS. Tissue pieces gently brushed to further remove villus epithelial cells, PBS replaced with 4% PFA and incubated at 4°C, gentle rocking for 2 hours. After two 10-minute washes with PBS, 3h incubation with 10% sucrose solution, then 16h with 20% sucrose + 10% glycerol solution (all gentle rocking, 4°C); tissues were rinsed once more with cold PBS and cut into approximately 1cm pieces. Blocking buffer (PBS + 5% donkey serum, 0.5% BSA, 0.3% Triton X, 0.1% NaN_3) was added for 3h (rocking 4°C) before primary antibodies added in blocking buffer for 5d. After 4 x 1h washes in wash buffer (PBS + 0.3% Triton X), secondary antibodies added in wash buffer for 12-16h (see Table S12 for primary and secondary antibodies used). Tissues washed in wash buffer (10x 30min, rocking 4°C) and dissected under dissection microscope into 1–2 villi-wide strips. Strips placed into C3eD clearing solution (described in ref [95]) for 30 minutes before mounting onto slides fitted with spacers using prolong diamond mounting medium (ThermoFisher). Images acquired on a Leica SP5 II confocal microscope running LAS-AF v2.7.3.9723 software (Leica), or a Zeiss LSM 780 confocal microscope running ZEN Black v14.0.27.201 (both Zeiss) using 10x and 20x objectives.

Whole-mount image quantification performed with FIJI (v.2.9.0). For ESM1 analysis, $ESM1^+$ cells counted in each villi and normalised to $CD31^+$ vascular villi area. VEGFR2 density/villi and number of branchpoints/villi were calculated using the 'Analyze skeleton' function in FIJI. Relative lacteal length calculated by lacteal length/villi length (as described in ref [94]. Lacteal filipodia/villi manually identified[94]. Leakage was quantified by counting areas of bead leakage in proximity to villi vessels, crypt vessels, or veins, and normalising to number of villi or veins per image respectively.

Quantitative single-cell imaging

HUVECs were seeded onto 384 well CellCarrier Ultra plates (Perkin Elmer), washed with Hanks Balanced Salt Solution (ThermoFisher) and changed to EBM-2 media (Lonza) + 2% FBS (Sigma) + penicillin/streptomycin (ThermoFisher) for 24h. Cells were treated with 100nM FICZ or DMSO control for 6h, and then fixed in 4% formaldehyde (Sigma) in PBS. Cells were permeabilised in PBS/0.5% TritonX-200 for 20 minutes, blocked in 1% BSA/PBS for 30 minutes and incubated with primary antibodies, diluted in blocking buffer, overnight at 4°C (phospho-Rb clone D20B12, Rb clone 4H1, p27 kip1 clone D37H1 – all Cell Signalling Technologies; E2F1 clone EPR3818(3) - Abcam). Cells were washed three times in PBS

followed by incubation with Alexa fluorophore labelled secondary antibodies, diluted 1:1000 in blocking buffer, for 1h at RT in the dark (goat anti-mouse IgG AlexaFluor488, Goat anti-rabbit IgG AlexaFluor568; both Invitrogen). Cells were washed three times in PBS and finally nuclei were labelled with 1µg/ml Hoechst 33258 diluted in PBS for 15min at RT, in the dark before a final three washes in PBS and storing the cells in PBS. Cells were imaged with a 10X N.A 0.4 objective on an Operetta CLS high-content microscope (PerkinElmer). Quantitative analysis of fixed cells was performed using Harmony software (PerkinElmer). Nuclei were segmented based on Hoechst intensity. Nuclei at the edge of the image were excluded. Fluorescence intensity of individual proteins and EdU was calculated within each nucleus. A threshold for EdU and phospho-Rb positive cells was calculated as in ref [96].

Statistical analysis

Statistical analyses were performed using GraphPad Prism 9 software. Statistical tests were used as follows: unpaired Student's *t* test and paired *t* tests to compare two groups; one-way ANOVA with Tukey's multiple comparisons tests, and two-way ANOVA with Šidák's multiple comparisons tests to compare multiple groups; and Gehan-Breslow-Wilcoxon tests to compare survival curves. We consider a *P* value of 0.05 significant. Significance levels of $*P < 0.05$, $**P < 0.01$, $***P < 0.001$, $****P < 0.0001$ used throughout.

Declarations

The authors declare no competing interests.

Data availability

All sequencing data (murine scRNAseq, murine RNAseq, and human RNAseq datasets) have been deposited in the NCBI gene expression omnibus as a superseries – accession number ***GSE201789*** (reviewer's token: mtmdwaqozbehxoz). All other flow cytometry, images and qPCR data are presented within the manuscript. Raw data is available from the corresponding authors upon reasonable request.

Acknowledgements

We first thank all staff at the Imperial College Central Biological Services for help with animal breeding, maintenance, and colony management, in particular S. Satchell and A. Miller for their invaluable assistance. We thank J. Elliot, B. Patel, and R. Maggio from the LMS/NIHR Imperial Biomedical Research Centre Flow Cytometry Facility for the support they provided in FACS; and L. Game, I. Andrew, and J. Haywood from the LMS Genomics team for assistance with sequencing. We are grateful to both the LMS microscopy team and Steve Rothery of the Imperial College FILM facility for their help with imaging and image analysis, I. Brodsky (University of Pennsylvania) for kindly providing kindly providing *Yptb*, and Evan Bieberstedt (Harvard University), for helpful discussions and troubleshooting with Pagoda2 analysis. This work was made possible through funding from the Wellcome Trust, Acteria, the Medical Research Council, the British Heart Foundation and Cancer Research UK.

Author contributions

BGW and CS conceived the project; BGW, CS,AB, JSG and GF designed experiments; BGW, AB and NG generated data; BGW, YFW, AB, NG, MD, and CC analysed data; YFW performed extensive scRNAseq analysis; MD and CC performed RNAseq analysis; BGW, CS, AB, YFW, JMVW, BP, ARB, GMB and AMR critically evaluated the data; BGW and CS wrote the manuscript; BGW, CS, YFW, AB, MD, CC and NG constructed figures; CS acquired funding and supervised the project; all authors reviewed the manuscript. YFW and AB are joint second authors. BGW is first and co-corresponding author.

References

1. Ricard, N., Bailly, S., Guignabert, C. & Simons, M. The quiescent endothelium: signalling pathways regulating organ-specific endothelial normalcy. *Nat Rev Cardiol* **18**, 565-580, doi:10.1038/s41569-021-00517-4 (2021).
2. Petrova, T. V. & Koh, G. Y. Organ-specific lymphatic vasculature: From development to pathophysiology. *J Exp Med* **215**, 35-49, doi:10.1084/jem.20171868 (2018).
3. Jurisic, G. & Detmar, M. Lymphatic endothelium in health and disease. *Cell Tissue Res* **335**, 97-108, doi:10.1007/s00441-008-0644-2 (2009).
4. Rajendran, P. *et al.* The vascular endothelium and human diseases. *Int J Biol Sci* **9**, 1057-1069, doi:10.7150/ijbs.7502 (2013).
5. Brulois, K. *et al.* A molecular map of murine lymph node blood vascular endothelium at single cell resolution. *Nat Commun* **11**, 3798, doi:10.1038/s41467-020-17291-5 (2020).
6. Gonzalez-Loyola, A. *et al.* FOXC2 controls adult lymphatic endothelial specialization, function, and gut lymphatic barrier preventing multiorgan failure. *Sci Adv* **7**, doi:10.1126/sciadv.abf4335 (2021).
7. Kalucka, J. *et al.* Single-Cell Transcriptome Atlas of Murine Endothelial Cells. *Cell* **180**, 764-779 e720, doi:10.1016/j.cell.2020.01.015 (2020).
8. Xiang, M. *et al.* A Single-Cell Transcriptional Roadmap of the Mouse and Human Lymph Node Lymphatic Vasculature. *Front Cardiovasc Med* **7**, 52, doi:10.3389/fcvm.2020.00052 (2020).
9. Stockinger, B., Shah, K. & Wincent, E. AHR in the intestinal microenvironment: safeguarding barrier function. *Nat Rev Gastroenterol Hepatol* **18**, 559-570, doi:10.1038/s41575-021-00430-8 (2021).
10. Kiss, E. A. *et al.* Natural aryl hydrocarbon receptor ligands control organogenesis of intestinal lymphoid follicles. *Science* **334**, 1561-1565, doi:10.1126/science.1214914 (2011).
11. Li, Y. *et al.* Exogenous stimuli maintain intraepithelial lymphocytes via aryl hydrocarbon receptor activation. *Cell* **147**, 629-640, doi:10.1016/j.cell.2011.09.025 (2011).
12. Schiering, C. *et al.* Feedback control of AHR signalling regulates intestinal immunity. *Nature* **542**, 242-245, doi:10.1038/nature21080 (2017).
13. Shah, K. *et al.* Cell-intrinsic Aryl Hydrocarbon Receptor signalling is required for the resolution of injury-induced colonic stem cells. *Nat Commun* **13**, 1827, doi:10.1038/s41467-022-29098-7 (2022).
14. Liu, J. Z. *et al.* Association analyses identify 38 susceptibility loci for inflammatory bowel disease and highlight shared genetic risk across populations. *Nat Genet* **47**, 979-986, doi:10.1038/ng.3359

(2015).

15. Metidji, A. *et al.* The Environmental Sensor AHR Protects from Inflammatory Damage by Maintaining Intestinal Stem Cell Homeostasis and Barrier Integrity. *Immunity* **49**, 353-362 e355, doi:10.1016/j.immuni.2018.07.010 (2018).
16. Lahvis, G. P. *et al.* Portosystemic shunting and persistent fetal vascular structures in aryl hydrocarbon receptor-deficient mice. *Proc Natl Acad Sci U S A* **97**, 10442-10447, doi:10.1073/pnas.190256997 (2000).
17. Lahvis, G. P. *et al.* The aryl hydrocarbon receptor is required for developmental closure of the ductus venosus in the neonatal mouse. *Mol Pharmacol* **67**, 714-720, doi:10.1124/mol.104.008888 (2005).
18. Thackaberry, E. A., Gabaldon, D. M., Walker, M. K. & Smith, S. M. Aryl hydrocarbon receptor null mice develop cardiac hypertrophy and increased hypoxia-inducible factor-1alpha in the absence of cardiac hypoxia. *Cardiovasc Toxicol* **2**, 263-274, doi:10.1385/ct:2:4:263 (2002).
19. Agbor, L. N., Elased, K. M. & Walker, M. K. Endothelial cell-specific aryl hydrocarbon receptor knockout mice exhibit hypotension mediated, in part, by an attenuated angiotensin II responsiveness. *Biochem Pharmacol* **82**, 514-523, doi:10.1016/j.bcp.2011.06.011 (2011).
20. Han, Z. *et al.* Aryl hydrocarbon receptor mediates laminar fluid shear stress-induced CYP1A1 activation and cell cycle arrest in vascular endothelial cells. *Cardiovasc Res* **77**, 809-818, doi:10.1093/cvr/cvm095 (2008).
21. McMillan, B. J. & Bradfield, C. A. The aryl hydrocarbon receptor is activated by modified low-density lipoprotein. *Proc Natl Acad Sci U S A* **104**, 1412-1417, doi:10.1073/pnas.0607296104 (2007).
22. Juan, S. H., Lee, J. L., Ho, P. Y., Lee, Y. H. & Lee, W. S. Antiproliferative and antiangiogenic effects of 3-methylcholanthrene, an aryl-hydrocarbon receptor agonist, in human umbilical vascular endothelial cells. *Eur J Pharmacol* **530**, 1-8, doi:10.1016/j.ejphar.2005.11.023 (2006).
23. Li, Y. *et al.* ITE Suppresses Angiogenic Responses in Human Artery and Vein Endothelial Cells: Differential Roles of AhR. *Reprod Toxicol* **74**, 181-188, doi:10.1016/j.reprotox.2017.09.010 (2017).
24. Li, Y., Zhou, C., Lei, W., Wang, K. & Zheng, J. Roles of aryl hydrocarbon receptor in endothelial angiogenic responsesdagger. *Biol Reprod* **103**, 927-937, doi:10.1093/biolre/ioaa128 (2020).
25. Fan, J. *et al.* Characterizing transcriptional heterogeneity through pathway and gene set overdispersion analysis. *Nat Methods* **13**, 241-244, doi:10.1038/nmeth.3734 (2016).
26. Van de Sande, B. *et al.* A scalable SCENIC workflow for single-cell gene regulatory network analysis. *Nat Protoc* **15**, 2247-2276, doi:10.1038/s41596-020-0336-2 (2020).
27. Vila Ellis, L. *et al.* Epithelial Vegfa Specifies a Distinct Endothelial Population in the Mouse Lung. *Dev Cell* **52**, 617-630 e616, doi:10.1016/j.devcel.2020.01.009 (2020).
28. Zhou, R. H. *et al.* Vascular endothelial growth factor activation of sterol regulatory element binding protein: a potential role in angiogenesis. *Circ Res* **95**, 471-478, doi:10.1161/01.RES.0000139956.42923.4A (2004).

29. Takao, K. *et al.* Deficiency of schnurri-2, an MHC enhancer binding protein, induces mild chronic inflammation in the brain and confers molecular, neuronal, and behavioral phenotypes related to schizophrenia. *Neuropsychopharmacology* **38**, 1409-1425, doi:10.1038/npp.2013.38 (2013).
30. Henderson, C. J. *et al.* Application of a novel regulatable Cre recombinase system to define the role of liver and gut metabolism in drug oral bioavailability. *Biochem J* **465**, 479-488, doi:10.1042/BJ20140582 (2015).
31. Alghamdi, A. A. A. *et al.* NRP2 as an Emerging Angiogenic Player; Promoting Endothelial Cell Adhesion and Migration by Regulating Recycling of alpha5 Integrin. *Front Cell Dev Biol* **8**, 395, doi:10.3389/fcell.2020.00395 (2020).
32. Bruhl, T. *et al.* p21Cip1 levels differentially regulate turnover of mature endothelial cells, endothelial progenitor cells, and in vivo neovascularization. *Circ Res* **94**, 686-692, doi:10.1161/01.RES.0000119922.71855.56 (2004).
33. Planel, S., Salomon, A., Jalinot, P., Feige, J. J. & Cherradi, N. A novel concept in antiangiogenic and antitumoral therapy: multitarget destabilization of short-lived mRNAs by the zinc finger protein ZFP36L1. *Oncogene* **29**, 5989-6003, doi:10.1038/onc.2010.341 (2010).
34. Yao, Y., Yao, J. & Bostrom, K. I. SOX Transcription Factors in Endothelial Differentiation and Endothelial-Mesenchymal Transitions. *Front Cardiovasc Med* **6**, 30, doi:10.3389/fcvm.2019.00030 (2019).
35. Guo, N. *et al.* Transcriptional regulation of neural stem cell expansion in the adult hippocampus. *Elife* **11**, doi:10.7554/eLife.72195 (2022).
36. Sporl, F. *et al.* Kruppel-like factor 9 is a circadian transcription factor in human epidermis that controls proliferation of keratinocytes. *Proc Natl Acad Sci U S A* **109**, 10903-10908, doi:10.1073/pnas.1118641109 (2012).
37. El Amri, M., Fitzgerald, U. & Schlosser, G. MARCKS and MARCKS-like proteins in development and regeneration. *J Biomed Sci* **25**, 43, doi:10.1186/s12929-018-0445-1 (2018).
38. Roh, H. C. *et al.* Simultaneous Transcriptional and Epigenomic Profiling from Specific Cell Types within Heterogeneous Tissues In Vivo. *Cell Rep* **18**, 1048-1061, doi:10.1016/j.celrep.2016.12.087 (2017).
39. Wang, Y. *et al.* Ephrin-B2 controls VEGF-induced angiogenesis and lymphangiogenesis. *Nature* **465**, 483-486, doi:10.1038/nature09002 (2010).
40. Kamba, T. *et al.* VEGF-dependent plasticity of fenestrated capillaries in the normal adult microvasculature. *Am J Physiol Heart Circ Physiol* **290**, H560-576, doi:10.1152/ajpheart.00133.2005 (2006).
41. Potente, M. & Makinen, T. Vascular heterogeneity and specialization in development and disease. *Nat Rev Mol Cell Biol* **18**, 477-494, doi:10.1038/nrm.2017.36 (2017).
42. Farr, L., Ghosh, S. & Moonah, S. Role of MIF Cytokine/CD74 Receptor Pathway in Protecting Against Injury and Promoting Repair. *Front Immunol* **11**, 1273, doi:10.3389/fimmu.2020.01273 (2020).

43. Heuberger, C., Pott, J. & Maloy, K. J. Why do intestinal epithelial cells express MHC class II? *Immunology* **162**, 357-367, doi:10.1111/imm.13270 (2021).
44. Luissint, A. C., Nusrat, A. & Parkos, C. A. JAM-related proteins in mucosal homeostasis and inflammation. *Semin Immunopathol* **36**, 211-226, doi:10.1007/s00281-014-0421-0 (2014).
45. Bernier-Latmani, J. *et al.* Apelin-driven endothelial cell migration sustains intestinal progenitor cells and tumor growth. *Nat Cardiovasc Res* **1**, 476-490, doi:10.1038/s44161-022-00061-5 (2022).
46. Bernier-Latmani, J. *et al.* ADAMTS18(+) villus tip telocytes maintain a polarized VEGFA signaling domain and fenestrations in nutrient-absorbing intestinal blood vessels. *Nat Commun* **13**, 3983, doi:10.1038/s41467-022-31571-2 (2022).
47. Rocha, S. F. *et al.* Esm1 modulates endothelial tip cell behavior and vascular permeability by enhancing VEGF bioavailability. *Circ Res* **115**, 581-590, doi:10.1161/CIRCRESAHA.115.304718 (2014).
48. Goncharov, N. V., Nadeev, A. D., Jenkins, R. O. & Avdonin, P. V. Markers and Biomarkers of Endothelium: When Something Is Rotten in the State. *Oxid Med Cell Longev* **2017**, 9759735, doi:10.1155/2017/9759735 (2017).
49. Rossi, E., Bernabeu, C. & Smadja, D. M. Endoglin as an Adhesion Molecule in Mature and Progenitor Endothelial Cells: A Function Beyond TGF-beta. *Front Med (Lausanne)* **6**, 10, doi:10.3389/fmed.2019.00010 (2019).
50. Cho, S. CD36 as a therapeutic target for endothelial dysfunction in stroke. *Curr Pharm Des* **18**, 3721-3730, doi:10.2174/138161212802002760 (2012).
51. Davis, K. M. All Yersinia Are Not Created Equal: Phenotypic Adaptation to Distinct Niches Within Mammalian Tissues. *Front Cell Infect Microbiol* **8**, 261, doi:10.3389/fcimb.2018.00261 (2018).
52. Barnes, P. D., Bergman, M. A., Mecsas, J. & Isberg, R. R. Yersinia pseudotuberculosis disseminates directly from a replicating bacterial pool in the intestine. *J Exp Med* **203**, 1591-1601, doi:10.1084/jem.20060905 (2006).
53. Medzhitov, R., Schneider, D. S. & Soares, M. P. Disease tolerance as a defense strategy. *Science* **335**, 936-941, doi:10.1126/science.1214935 (2012).
54. Spadoni, I. *et al.* A gut-vascular barrier controls the systemic dissemination of bacteria. *Science* **350**, 830-834, doi:10.1126/science.aad0135 (2015).
55. Kalucka, J. *et al.* Quiescent Endothelial Cells Upregulate Fatty Acid beta-Oxidation for Vasculoprotection via Redox Homeostasis. *Cell Metab* **28**, 881-894 e813, doi:10.1016/j.cmet.2018.07.016 (2018).
56. Mizee, M. R. *et al.* Retinoic acid induces blood-brain barrier development. *J Neurosci* **33**, 1660-1671, doi:10.1523/JNEUROSCI.1338-12.2013 (2013).
57. Lu, M. M., Li, S., Yang, H. & Morrisey, E. E. Foxp4: a novel member of the Foxp subfamily of winged-helix genes co-expressed with Foxp1 and Foxp2 in pulmonary and gut tissues. *Mech Dev* **119 Suppl 1**, S197-202, doi:10.1016/s0925-4773(03)00116-3 (2002).

58. Wiehagen, K. R. *et al.* Foxp4 is dispensable for T cell development, but required for robust recall responses. *PLoS One* **7**, e42273, doi:10.1371/journal.pone.0042273 (2012).
59. Fan, Y. *et al.* Kruppel-like factors and vascular wall homeostasis. *J Mol Cell Biol* **9**, 352-363, doi:10.1093/jmcb/mjx037 (2017).
60. Tisch, N. *et al.* Caspase-8 in endothelial cells maintains gut homeostasis and prevents small bowel inflammation in mice. *EMBO Mol Med* **14**, e14121, doi:10.15252/emmm.202114121 (2022).
61. Pang, P. H. *et al.* Molecular mechanisms of p21 and p27 induction by 3-methylcholanthrene, an aryl-hydrocarbon receptor agonist, involved in antiproliferation of human umbilical vascular endothelial cells. *J Cell Physiol* **215**, 161-171, doi:10.1002/jcp.21299 (2008).
62. Bernier-Latmani, J. *et al.* DLL4 promotes continuous adult intestinal lacteal regeneration and dietary fat transport. *J Clin Invest* **125**, 4572-4586, doi:10.1172/JCI82045 (2015).
63. Hong, S. P. *et al.* Distinct fibroblast subsets regulate lacteal integrity through YAP/TAZ-induced VEGF-C in intestinal villi. *Nat Commun* **11**, 4102, doi:10.1038/s41467-020-17886-y (2020).
64. Maharaj, A. S., Saint-Geniez, M., Maldonado, A. E. & D'Amore, P. A. Vascular endothelial growth factor localization in the adult. *Am J Pathol* **168**, 639-648, doi:10.2353/ajpath.2006.050834 (2006).
65. Kimura, A. *et al.* Aryl hydrocarbon receptor in combination with Stat1 regulates LPS-induced inflammatory responses. *J Exp Med* **206**, 2027-2035, doi:10.1084/jem.20090560 (2009).
66. Yamada, T. *et al.* Constitutive aryl hydrocarbon receptor signaling constrains type I interferon-mediated antiviral innate defense. *Nat Immunol* **17**, 687-694, doi:10.1038/ni.3422 (2016).
67. Bessede, A. *et al.* Aryl hydrocarbon receptor control of a disease tolerance defence pathway. *Nature* **511**, 184-190, doi:10.1038/nature13323 (2014).
68. Young, M. R. Endothelial cells in the eyes of an immunologist. *Cancer Immunol Immunother* **61**, 1609-1616, doi:10.1007/s00262-012-1335-0 (2012).
69. Dryden, N. H. *et al.* The transcription factor Erg controls endothelial cell quiescence by repressing activity of nuclear factor (NF)-kappaB p65. *J Biol Chem* **287**, 12331-12342, doi:10.1074/jbc.M112.346791 (2012).
70. Shah, A. V. *et al.* The endothelial transcription factor ERG mediates Angiopoietin-1-dependent control of Notch signalling and vascular stability. *Nat Commun* **8**, 16002, doi:10.1038/ncomms16002 (2017).
71. Wilhelm, K. *et al.* FOXO1 couples metabolic activity and growth state in the vascular endothelium. *Nature* **529**, 216-220, doi:10.1038/nature16498 (2016).
72. Rafii, S., Butler, J. M. & Ding, B. S. Angiocrine functions of organ-specific endothelial cells. *Nature* **529**, 316-325, doi:10.1038/nature17040 (2016).
73. Naito, H. *et al.* TAK1 Prevents Endothelial Apoptosis and Maintains Vascular Integrity. *Dev Cell* **48**, 151-166 e157, doi:10.1016/j.devcel.2018.12.002 (2019).
74. De Juan, A. & Segura, E. Modulation of Immune Responses by Nutritional Ligands of Aryl Hydrocarbon Receptor. *Front Immunol* **12**, 645168, doi:10.3389/fimmu.2021.645168 (2021).

75. Wu, N. *et al.* MAP3K2-regulated intestinal stromal cells define a distinct stem cell niche. *Nature* **592**, 606-610, doi:10.1038/s41586-021-03283-y (2021).
76. Sun, X. *et al.* Flow cytometric analysis of T lymphocyte proliferation in vivo by EdU incorporation. *Int Immunopharmacol* **41**, 56-65, doi:10.1016/j.intimp.2016.10.019 (2016).
77. Shaw, T. N. *et al.* Tissue-resident macrophages in the intestine are long lived and defined by Tim-4 and CD4 expression. *J Exp Med* **215**, 1507-1518, doi:10.1084/jem.20180019 (2018).
78. Yu, Y. R. *et al.* A Protocol for the Comprehensive Flow Cytometric Analysis of Immune Cells in Normal and Inflamed Murine Non-Lymphoid Tissues. *PLoS One* **11**, e0150606, doi:10.1371/journal.pone.0150606 (2016).
79. Stuart, T. *et al.* Comprehensive Integration of Single-Cell Data. *Cell* **177**, 1888-1902 e1821, doi:10.1016/j.cell.2019.05.031 (2019).
80. Ilicic, T. *et al.* Classification of low quality cells from single-cell RNA-seq data. *Genome Biol* **17**, 29, doi:10.1186/s13059-016-0888-1 (2016).
81. Hafemeister, C. & Satija, R. Normalization and variance stabilization of single-cell RNA-seq data using regularized negative binomial regression. *Genome Biol* **20**, 296, doi:10.1186/s13059-019-1874-1 (2019).
82. McGinnis, C. S., Murrow, L. M. & Gartner, Z. J. DoubletFinder: Doublet Detection in Single-Cell RNA Sequencing Data Using Artificial Nearest Neighbors. *Cell Syst* **8**, 329-337 e324, doi:10.1016/j.cels.2019.03.003 (2019).
83. Xie, Z. *et al.* Gene Set Knowledge Discovery with Enrichr. *Curr Protoc* **1**, e90, doi:10.1002/cpz1.90 (2021).
84. Aibar, S. *et al.* SCENIC: single-cell regulatory network inference and clustering. *Nat Methods* **14**, 1083-1086, doi:10.1038/nmeth.4463 (2017).
85. Suo, S. *et al.* Revealing the Critical Regulators of Cell Identity in the Mouse Cell Atlas. *Cell Rep* **25**, 1436-1445 e1433, doi:10.1016/j.celrep.2018.10.045 (2018).
86. Gu, Z., Eils, R. & Schlesner, M. Complex heatmaps reveal patterns and correlations in multidimensional genomic data. *Bioinformatics* **32**, 2847-2849, doi:10.1093/bioinformatics/btw313 (2016).
87. Dobin, A. *et al.* STAR: ultrafast universal RNA-seq aligner. *Bioinformatics* **29**, 15-21, doi:10.1093/bioinformatics/bts635 (2013).
88. Love, M. I., Huber, W. & Anders, S. Moderated estimation of fold change and dispersion for RNA-seq data with DESeq2. *Genome Biol* **15**, 550, doi:10.1186/s13059-014-0550-8 (2014).
89. Risso, D., Ngai, J., Speed, T. P. & Dudoit, S. Normalization of RNA-seq data using factor analysis of control genes or samples. *Nat Biotechnol* **32**, 896-902, doi:10.1038/nbt.2931 (2014).
90. Mootha, V. K. *et al.* PGC-1alpha-responsive genes involved in oxidative phosphorylation are coordinately downregulated in human diabetes. *Nat Genet* **34**, 267-273, doi:10.1038/ng1180 (2003).

91. Subramanian, A. *et al.* Gene set enrichment analysis: a knowledge-based approach for interpreting genome-wide expression profiles. *Proc Natl Acad Sci U S A* **102**, 15545-15550, doi:10.1073/pnas.0506580102 (2005).
92. Kim, D. *et al.* TopHat2: accurate alignment of transcriptomes in the presence of insertions, deletions and gene fusions. *Genome Biol* **14**, R36, doi:10.1186/gb-2013-14-4-r36 (2013).
93. Liao, Y., Smyth, G. K. & Shi, W. featureCounts: an efficient general purpose program for assigning sequence reads to genomic features. *Bioinformatics* **30**, 923-930, doi:10.1093/bioinformatics/btt656 (2014).
94. Bernier-Latmani, J. & Petrova, T. V. High-resolution 3D analysis of mouse small-intestinal stroma. *Nat Protoc* **11**, 1617-1629, doi:10.1038/nprot.2016.092 (2016).
95. Li, W., Germain, R. N. & Gerner, M. Y. High-dimensional cell-level analysis of tissues with Ce3D multiplex volume imaging. *Nat Protoc* **14**, 1708-1733, doi:10.1038/s41596-019-0156-4 (2019).
96. Pennycook, B. R. & Barr, A. R. Palbociclib-mediated cell cycle arrest can occur in the absence of the CDK inhibitors p21 and p27. *Open Biol* **11**, 210125, doi:10.1098/rsob.210125 (2021).

Supplementary Information

Supplementary Tables S1-S11 and Extended Figure 9 are not available with this version.

Figures

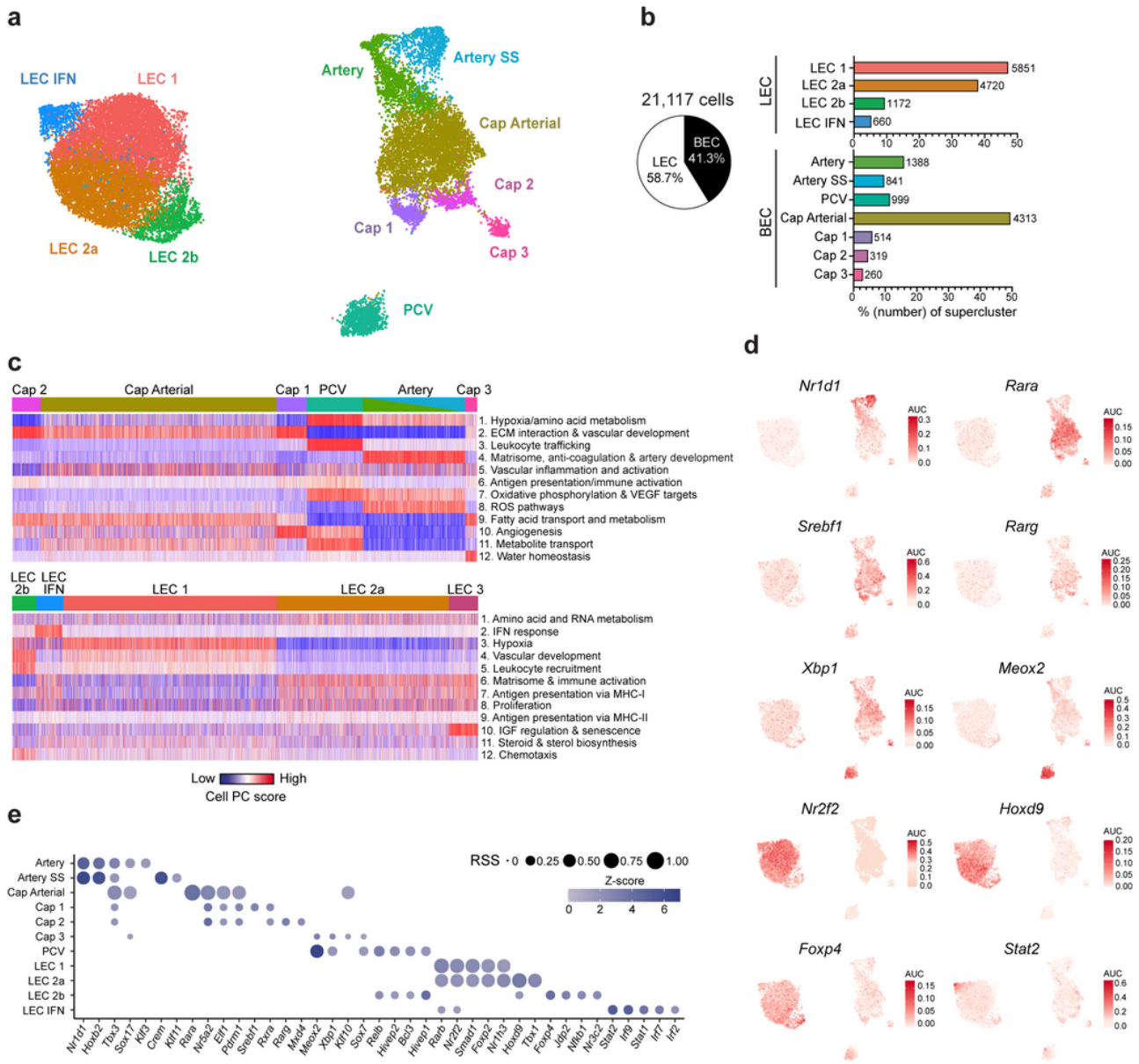

Figure 1

Single cell transcriptomics reveals the cellular complexity of enteric vasculature.

a, Uniform manifold approximation and projection (UMAP) of small intestinal ECs, showing data structure and identified clusters **b**, Breakdown of cell numbers and proportional representation. Pie chart shows % of BEC and LEC superclusters of initial 21,117 cells post-filtering, QC analysis and doublet removal. Bar charts show %/cell numbers within each cluster, of parent supercluster. **c**, Subclustering into

BEC and LEC for geneset-focused overdispersion analysis using Pagoda2. Heatmap shows principal component (PC)/aspect scores for each cell in the data, assigned based on level of statistical enrichment within curated endothelial-related input genesets (see methods and supplementary Table 3). Genesets clustered together based on similarities within constituent genes and similar patterns of cell separation to create aspects (heatmap rows, see also supplementary Table 4). Top 12 aspects manually annotated based on top constituent pathways. **d**, Transcription factor network activity AUC score distributions of selected top enriched regulons for each cluster following SCENIC analysis. **e**, Top 5 enriched regulons, by regulon specificity score (RSS), for each of the clusters. RSS and normalised regulon activity (z-score) shown.

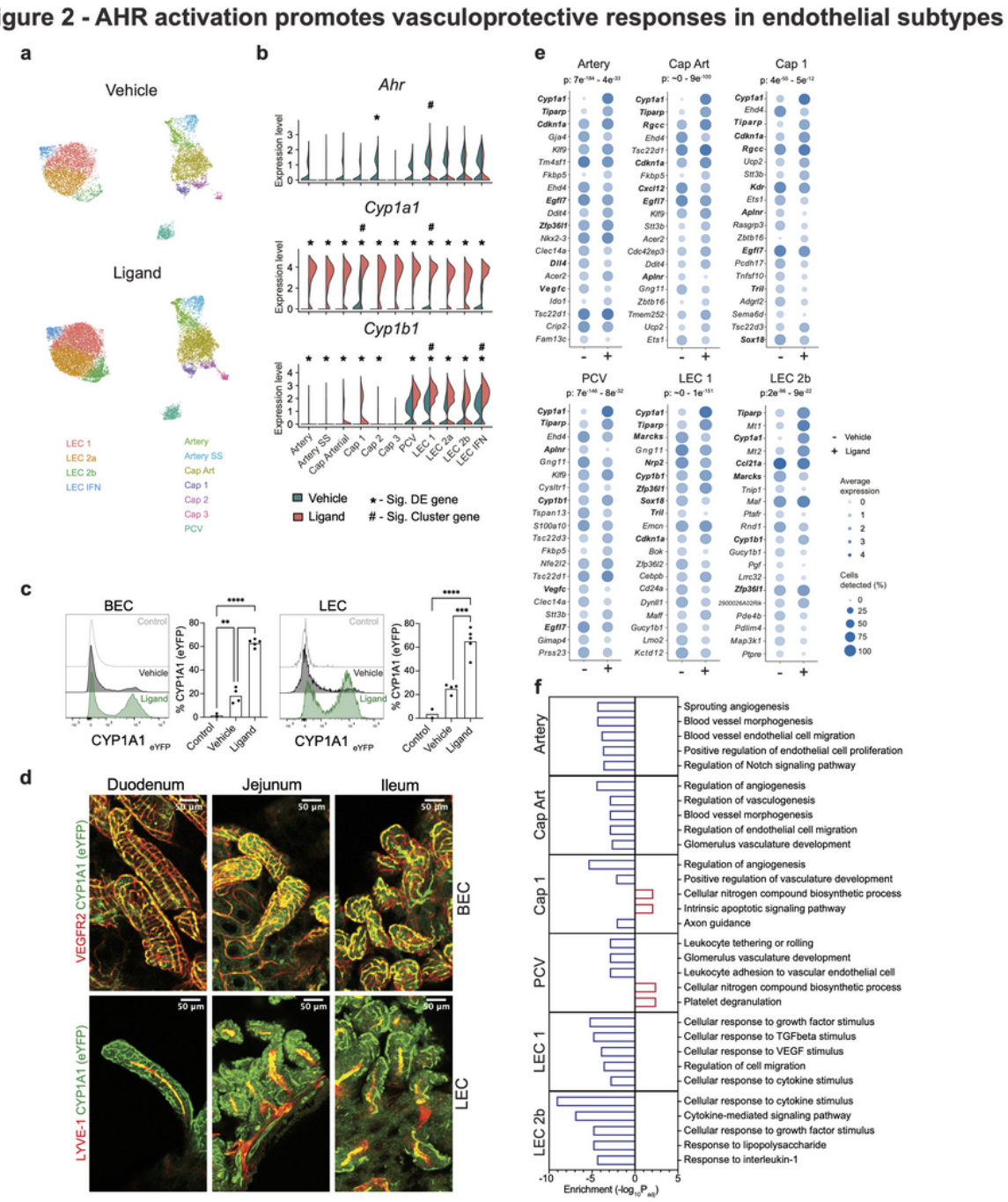

Figure 2

AHR activation promotes vasculoprotective responses in endothelial subtypes.

a, UMAP plots split by condition (vehicle treated, or treated i.p. with AHR ligand FICZ for 3h) **b**, Expression of *Ahr*, *Cyp1a1*, and *Cyp1b1* across the clusters shown as split violin plot (vehicle – blue, ligand-treated – red). * denotes significant DE gene (padj<0.05), # denotes conserved marker enriched in indicated cluster

(padj<0.05). **c**, *Cyp1a1*-eYFP expression within BEC or LEC isolated from *Cyp1a1*-reporter mice following treatment with AHR ligand 3-methylcholanthrene (3-MC), vehicle control, or (3-MC-treated) non-reporter control. Bars show the mean, symbols represent individual mice. **d**, Representative whole-mount gut staining of gut sections in *Cyp1a1*-reporter mice 5-days post 3-MC administration. VEGFR2 and LYVE-1 stain for BEC and LEC respectively. **e**, Dot plots of top 20 differentially expressed (DE) genes for 6 selected scRNAseq clusters in ligand-treated (+) and vehicle-treated (-) conditions, sorted by adjusted p value (colour intensity = average expression level, dot size = average % expression) Adjusted p value range for each cluster shown above plots. Genes relating to canonical AHR pathway, or proliferation in bold. **f**, Top 5 enriched genesets in ligand-treated mice for each of these 6 clusters (GO Biological Processes). Upregulated, and downregulated genesets separately tested and top 5 enrichment scores for both comparisons combined shown. ** $P < 0.01$, *** $P < 0.001$, **** $P < 0.0001$ as calculated by one-way ANOVA with Tukey's multiple comparisons tests.

Figure 3 - AHR ligands act directly on ECs to promote quiescence and anti-inflammatory programs.

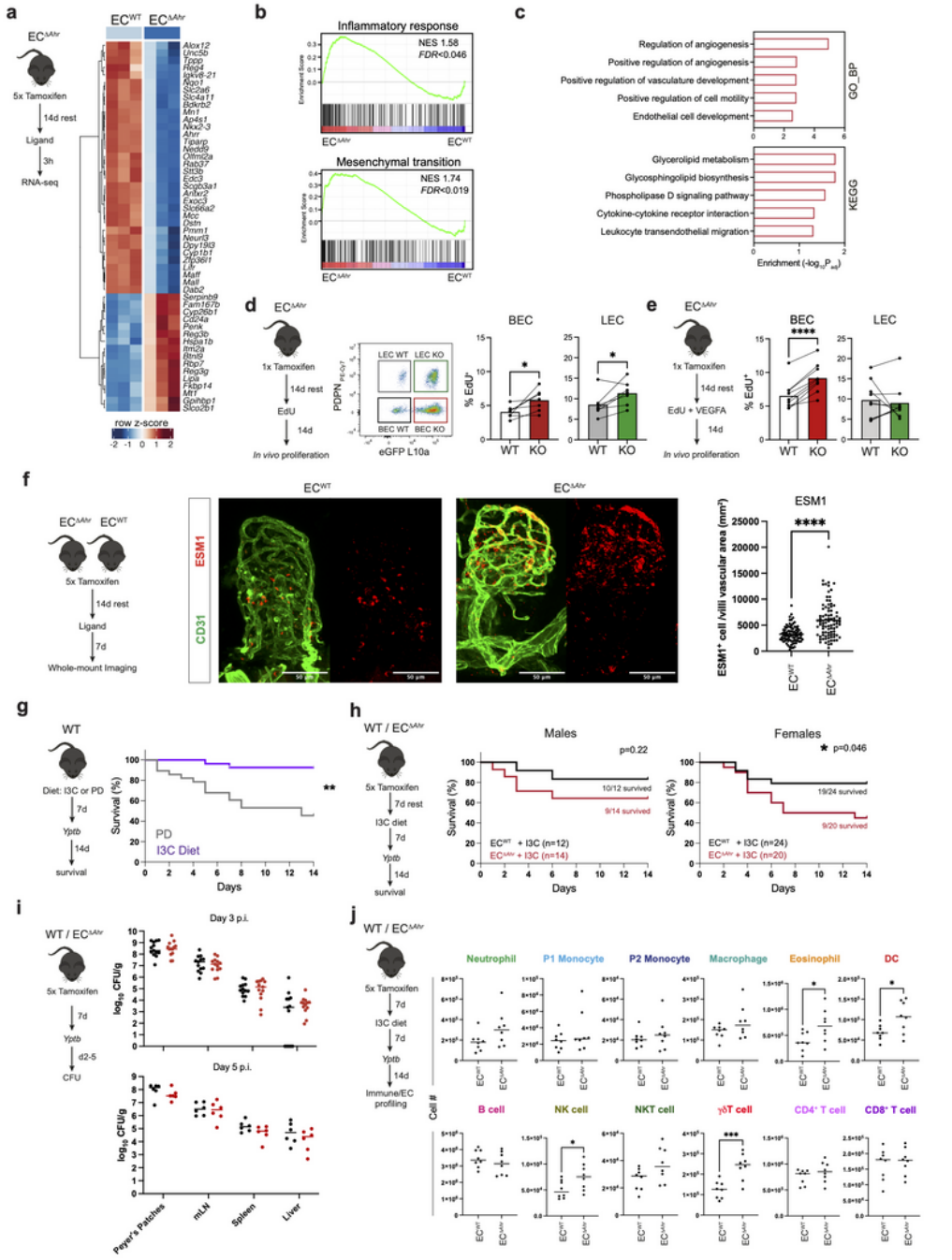

Figure 3

AHR ligands act directly on ECs to promote quiescence and anti-inflammatory programs.

a, Wild-type (EC^{WT}) and mice with endothelial-specific Ahr deletion ($EC^{D\Delta hr}$) were treated intraperitoneally (i.p.) with AHR ligand FICZ for 3hrs followed by EC sorting and bulk RNA-seq from the small intestine. Relative expression of top 50 differentially expressed genes (by adjusted p value) between *Ahr*-deficient

($EC^{D\Delta hr}$) and *Ahr* WT (EC^{WT}) small intestinal BEC, sorted by adjusted p value. **b**, Barcode plots showing geneset enrichment analysis (GSEA) on selected hallmark genesets (NES, normalised enrichment score; FDR, false discovery rate). **c**, BEC top 5 biological processes and KEGG genesets upregulated in $EC^{D\Delta hr}$ compared to EC^{WT}. **d**, After single-dose tamoxifen (to suboptimally delete *Ahr* within ECs) $EC^{D\Delta hr}$ mice were given EdU in drinking water for 14d. WT and AHR-deficient (KO) BEC and LEC within same animals were compared for proliferation by EdU detection (% of EdU^+ BEC or LEC shown, n=7/group). Connected lines show matched individual data, bar heights represent means. **e,** Following suboptimal AHR depletion in $EC^{D\Delta hr}$ mice, animals were treated with bi-weekly VEGFA injections during the 2 week EdU course. Proliferation detected and presented as in part d (n=9/group). **f,** Fully AHR-depleted $EC^{D\Delta hr}$ or EC^{WT} mice were treated with 3-MC, and 7d later gut villi vasculature analysed for ESM1 expression (red) within the villi vasculature ($CD31^+$, green). Representative images and quantification of $ESM1^+$ cells normalised to villi vasculature area between groups (EC^{WT} n=85 villi, $EC^{D\Delta hr}$ n=88 villi, points represent individual villi combined from 4 mice/group, bar heights represent means). **g**, Survival curve comparing *Yptb*-infected WT mice fed with purified diet (PD; n=12) or purified diet containing I3C (I3C; n=12). Data combined from 2 individual experiments. **h,** Survival curves of I3C-diet-fed $EC^{D\Delta hr}$ and EC^{WT} male and female mice after *Yptb* infection (5×10^7 CFU/mouse). Data combined from 2-3 independent cohorts for each male and female mice. Animal numbers indicated in inset on plots and p-values given above each plot. **i,** CFU determination in 4 tissues days 3 and 5 after infection of $EC^{D\Delta hr}$ and EC^{WT} mice with *Yptb* (5×10^8 CFU/mouse). Dots show individual mice, lines show mean values (day 3 – n=13/group, 2 independent experiments; day 5 – 6/group, 1 independent experiment). **j,** Immune cell profiling in SI lamina propria 3 days after infection (5×10^7 CFU/mouse). Data shows total cell numbers of 10 immune cell populations (gated as shown in Extended Data Figure 6a, and Extended Data Figure 8d). n=8/group, dots represent individual mice, lines show means. *P<0.05, **P < 0.01, ***P < 0.001, ****P<0.0001, as calculated by paired t-tests (**d-e, g**), unpaired t-tests (**f, i-j**), or by Gehan-Breslow-Wilcoxon tests (**g-h**).

Figure 4 - AHR facilitates vasculoprotective pathways in human ECs

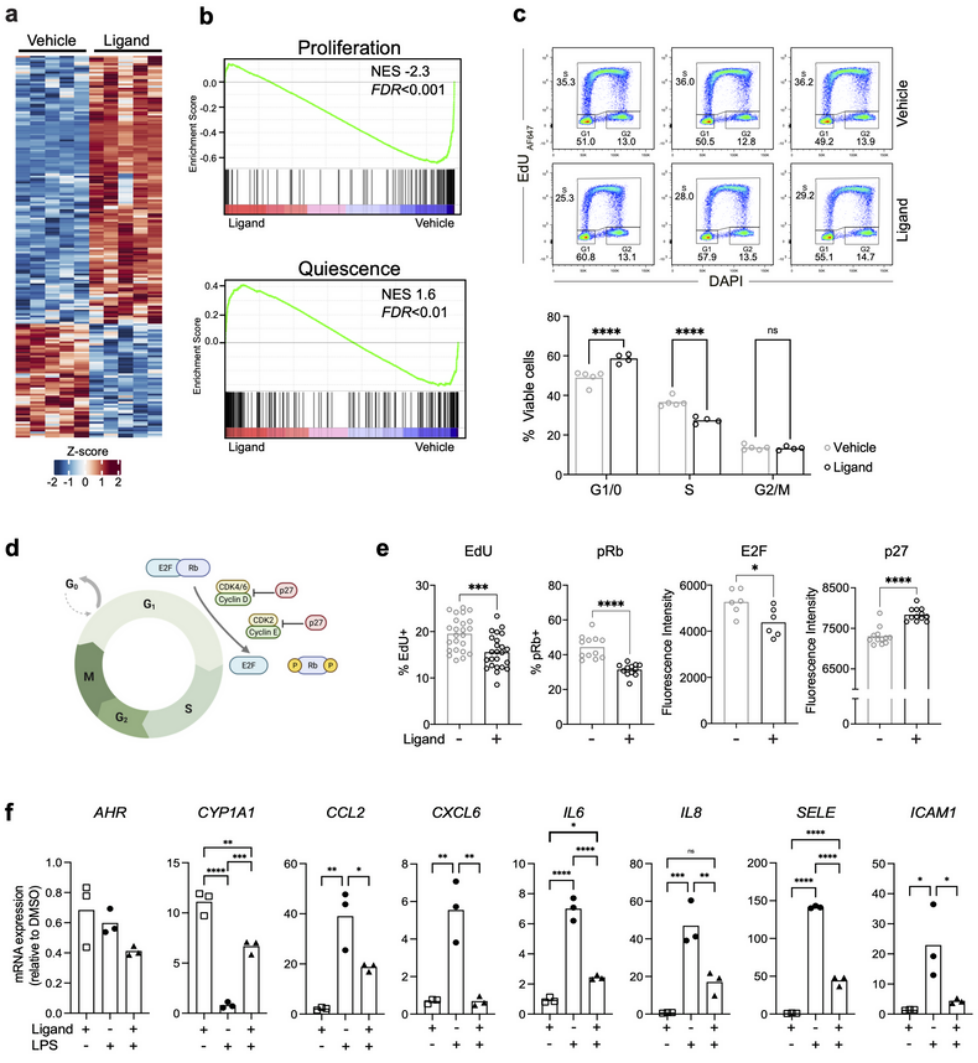

Figure 4

AHR facilitates vasculoprotective pathways in human ECs.

a, Heatmap showing unsupervised hierarchical clustering of DE genes following bulk RNAseq of FICZ treated HUVECs compared to HUVECs treated with vehicle (n=5/group). **b,** Enrichment plots showing GSEA using custom HUVEC-specific proliferation and quiescence gene sets (NES, normalised enrichment score; FDR, false discovery rate). **c,** Flow cytometric cell cycle analysis on HUVECs treated with 100nM FICZ for 6h compared to DMSO vehicle control. **d,** Schematic of cell cycle regulators (created using Biorender). **e,** Single-cell imaging of cell cycle regulators in 100nM FICZ treated (+) or vehicle-treated (-) HUVECs. Each symbol represents average expression from individual wells. **f**, HUVECs were treated with 100nM FICZ (2h), followed by LPS stimulation (4h) and profiled for expression (qPCR) of AHR pathway

genes and endothelial inflammatory markers. Data representative of 3 independent experiments. Data representative of 3 independent experiments. Bar heights show means throughout. *P<0.05, ** $P < 0.01$, *** $P < 0.001$, **** $P < 0.0001$ as calculated by two-way ANOVA with Šidák's multiple comparisons tests (**c**), unpaired t tests (**e**), and one-way ANOVA with Tukey's multiple comparison tests(**f**).

Supplementary Files

This is a list of supplementary files associated with this preprint. Click to download.

- WigginsetalExtendedDatafiguresR1page0001.jpg
- WigginsetalExtendedDatafiguresR1page0002.jpg
- WigginsetalExtendedDatafiguresR1page0003.jpg
- WigginsetalExtendedDatafiguresR1page0004.jpg
- WigginsetalExtendedDatafiguresR1page0005.jpg
- WigginsetalExtendedDatafiguresR1page0006.jpg
- WigginsetalExtendedDatafiguresR1page0007.jpg
- WigginsetalExtendedDatafiguresR1page0008.jpg
- TableS12.docx